

See discussions, stats, and author profiles for this publication at: <https://www.researchgate.net/publication/284982146>

Analysis of masonry structures with interface elements

Article · January 1994

CITATIONS

103

READS

2,394

1 author:



Paulo B. Lourenco

University of Minho

1,448 PUBLICATIONS 35,124 CITATIONS

SEE PROFILE

Delft University of Technology
Faculty of Civil Engineering

**ANALYSIS OF MASONRY STRUCTURES
WITH INTERFACE ELEMENTS**

THEORY AND APPLICATIONS

Author : P. B. LOURENÇO
Date : June 1994

TU-DELFT report no. 03-21-22-0-01
TNO-BOUW report no. 94-NM-R0762

**TNO Building and Construction Research
Computational Mechanics**

Summary

The use of numerical methods for the analysis of masonry structures has been extremely limited due to the large number of influence factors. To achieve a more fundamental insight in the behaviour of masonry a combined experimental and numerical research programme was started in the Netherlands. The present report contains the results of micro-modelling analyses, in which both masonry components are discretised. An interface cap model is developed as a part of a rational unit-joint model able to describe cracking, slip and crushing of the material. The new model is implemented in modern plasticity concepts including Euler backward return mapping strategies and consistent tangent operators for all modes of the composite yield surface. The parameters necessary to define the model are derived from micro-experiments.

To appraise the validity of the model, different tests results available in the literature are analysed.

Acknowledgements

The author wishes to express his gratitude to Dr. ir. J.G. Rots for his support during the course of this work. Illuminating discussions with Dr. ir. P. Feenstra about plasticity models and algorithms are also acknowledged as well as his useful suggestions on the final manuscript.

The financial support by the Netherlands Technology Foundation (STW) under grant DCT-33.3052 and by the Netherlands brick industries via the Center for Civil Engineering Research, Codes and Specifications (CUR) committees C96 and A33 on Structural Masonry, is gratefully acknowledged.

The calculations have been carried out with the Finite Element Package DIANA of TNO Building and Construction Research on Silicon Graphics Indigo R4000 and R4400 workstations of the Delft University of Technology.

1. INTRODUCTION

Masonry is a material which exhibits distinct directional properties due to the mortar joints which act as planes of weakness. The large number of influence factors, such as anisotropy of units, dimension of units, joint width, material properties of the units and mortar, arrangement of bed as well as head joints and quality of workmanship, make the simulation of masonry structures extremely difficult. To achieve a more fundamental insight in the behaviour of masonry and permit more competitive use of masonry, the combined analytical, experimental and numerical research programme *STRUCTURAL MASONRY* was initiated in the Netherlands in 1989. The aim of this programme is the provision of a rational basis for design rules, enabling modifications, additions and extrapolations of the existing Masonry Codes. The objective of the current work is less ambitious and essentially fundamental: to develop a reliable tool for the analysis and design of masonry structures.

In this report attention will be given to micro-models, wherein masonry components are modelled separately. Interface elements are used as potential crack, slip or crushing planes. A new interface cap model able to capture all masonry failure mechanisms is described. Unconditionally stable Euler backward algorithms are derived for all modes of the cap model. The Euler backward return mapping is solved with use of a local Newton-Raphson method. Tangent operators consistent with the integration algorithm are presented, including a correct handling of the corners. The model is formulated in the context of non-associated plasticity leading to nonsymmetric consistent tangent moduli.

To assess the performance of the model, experimental and numerical results on solid and hollow shear-walls, tested in the frame of the *STRUCTURAL MASONRY* project, are compared. This allows a clear understanding of the walls structural behaviour, flow of internal forces and redistribution of stresses in the pre- and post-peak regime. The parameters necessary to characterize the model are determined from available micro-experiments. One additional numerical simulation of a masonry deep beam test reported in available bibliography is also included.

2. EXPERIMENTAL BEHAVIOUR OF MASONRY AND ITS COMPONENTS

An accurate masonry description needs a complete set of experimental data. In the research programme described earlier micro-experiments have been carried out to fully characterize masonry as well as its components. Consequently, sufficient data are becoming available for a powerful iterative procedure capable of reproducing the behaviour of masonry. Van der Pluijm and Vermeltfoort (van der Pluijm and Vermeltfoort 1991, van der Pluijm 1992a, van der Pluijm 1992b and Vermeltfoort 1991) carried out tension, compression and shear tests on the components of masonry and on small masonry specimens, consisting of only a few units and joints. Different solid units were tested - soft mud clay bricks (Vijf Eiken - VE), wire cut bricks (Joosten - JO) and calcium silicate blocks (CS) - in combination with two different types of mortar - mortar B, 1:2:9 (cement:lime:sand, by volume) and mortar C, 1: $\frac{1}{2}$:4 $\frac{1}{2}$. Different combinations unit/mortar were tested and they will be referred in the form Unit.Mortar (for example JO.B for a test with Joosten wire cut brick and mortar B). The samples were tested in displacement-control with proper boundary conditions in order to obtain the deformation and strength properties, including the post-peak softening regime. These experiments resulted in the parameters described below.

2.1 Uniaxial compressive behaviour

Samples made only of units, ground and connected with an extremely thin layer of glue, and samples made of units and 10 mm mortar layers were tested (see Fig. 1). These samples of approximately the same size permit the calculation of the elastic modulae of both unit and mortar. In fact, the deformational characteristics of the units cannot be measured on a masonry specimen as shown by Vermeltfoort and van der Pluijm (1991). The deformation of the units measured at the outside of the specimen was much smaller than expected on the basis of a plane sections hypothesis due to a non-uniform distribution of stresses. Also the characteristics of the mortar embedded in the joint differ considerably from the characteristics of the mortar measured in mortar prisms. For this reason an experimental programme capable of measuring the triaxial state of masonry disks with a height of 12 mm extracted from the joints was recently setup by Bierwirth *et al.* (1993). The process proposed by Vermeltfoort and van der Pluijm (1991) is simpler but allows the calculation of the deformability characteristics for both components. The mortar deformability can be easily obtained by subtracting the brick deformability (available from the ground bricks test) to the total masonry deformability (obtained from the masonry specimen).

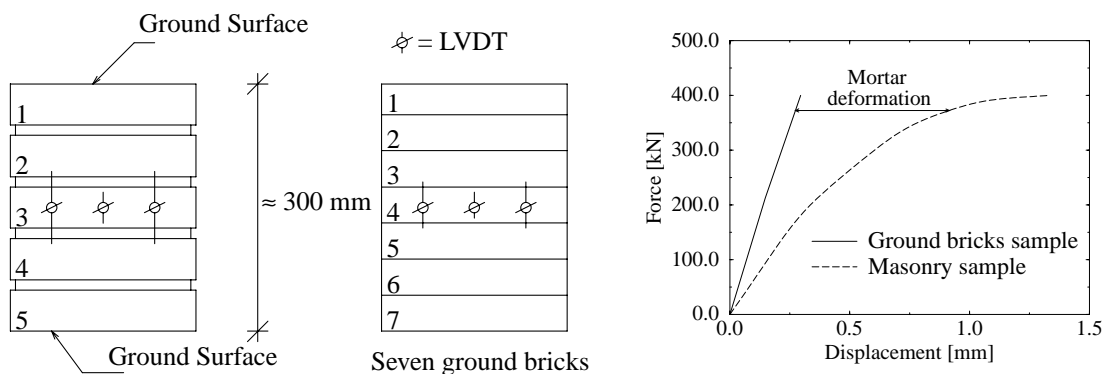


Fig. 1 - Stress-strain relations for masonry (including test samples)

The masonry specimen was loaded until failure but stress-strain diagrams are available only in the pre-peak regime. Some data about the post-peak regime do exist (Atkinson and Yan 1990, Priestley and Elder 1983). The results of these authors must be carefully analysed because compressive failure is a localized phenomena (Vonk 1992) and a energy based criterion must be established instead of a stress-strain relation.

The size effect is difficult to appraise but Vermeltfoort and Raijmakers (1993) pointed out that the values obtained for the Young's modulus of the specimens are $\approx 50\%$ higher than the values measured in large walls. Owing to the small size of the masonry specimens (one unit width and five units height) prisms cannot be considered as assemblages and therefore fully representative. Also, the influence of the specimen size on the ultimate compressive strength will not be analysed here and the reader is referred to Drysdale and Wong (1985) and Maurenbrecker (1980) for further discussion.

2.2 Mortar uniaxial tensile behaviour

Deformation controlled tests were carried out on masonry specimens (Fig. 2). These tests resulted in an exponential tension softening curve with a mode I fracture energy G_f^I in the range 0.005-0.02 N/mm, according to the unit/mortar combination. This fracture energy is defined as the amount of energy to create one unit area of a crack along the brick-mortar interface. It is equal to the area under the tension softening curve for a discrete crack. The values given above result from an extrapolation of the measured net bond surface of the specimen to the assumed net bond surface of the wall, neglecting any influence of the vertical joints (see Fig. 3);

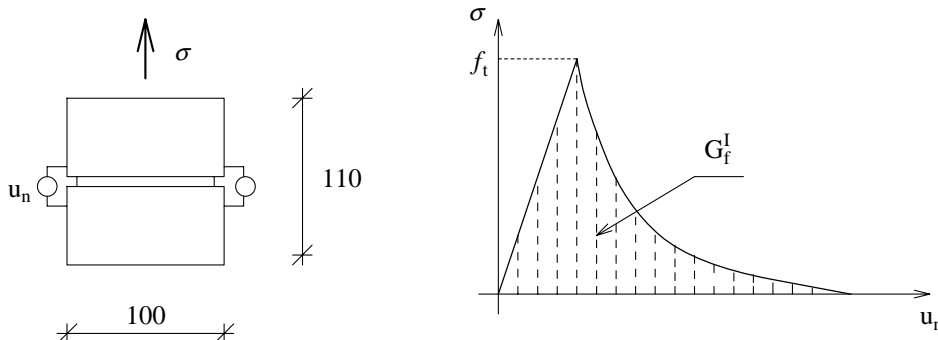
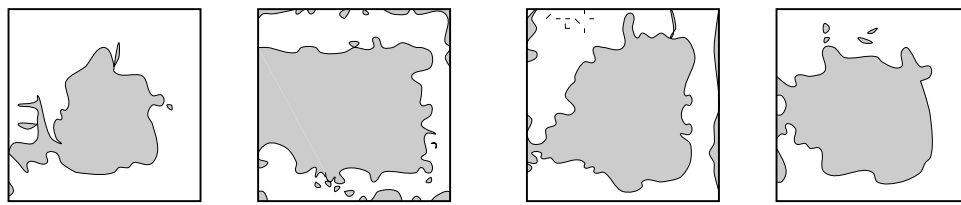


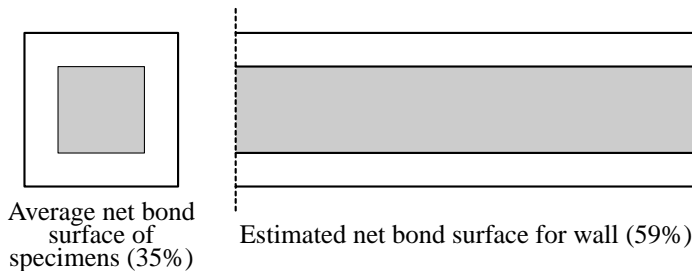
Fig. 2 - Test set-up to determine tension-softening curve and G_f^I for discrete crack

2.3 Unit tensile uniaxial behaviour

Uniaxial tensile tests in longitudinal and transverse directions were also carried out for the units. Thus, the values of the tensile strength and mode I fracture energy in both directions are available and can be found in van der Pluijm and Vermeltfoort (1991).



a) Net bond surface of VE.B tensile specimens (Van der Pluijm 1992a)



b) Extrapolation of bond surface from specimen to wall

Fig. 3 - Tensile bond surface

2.4 Shear behaviour

Similar tests were carried out with masonry shear specimens (Fig. 4). The confining stresses were applied with three different levels, $| -0.1 |$ MPa, $| -0.5 |$ MPa and $| -1.0 |$ MPa. The test apparatus did not allow application of tensile confining stresses and even for low compressive confining stresses very brittle results are found with potential instability of the test set-up. Noteworthy, for several specimens with higher confining stresses shearing of the interface unit/mortar was accompanied by diagonal cracking in the unit. The importance of mortar/brick interaction will be discussed later in this report.

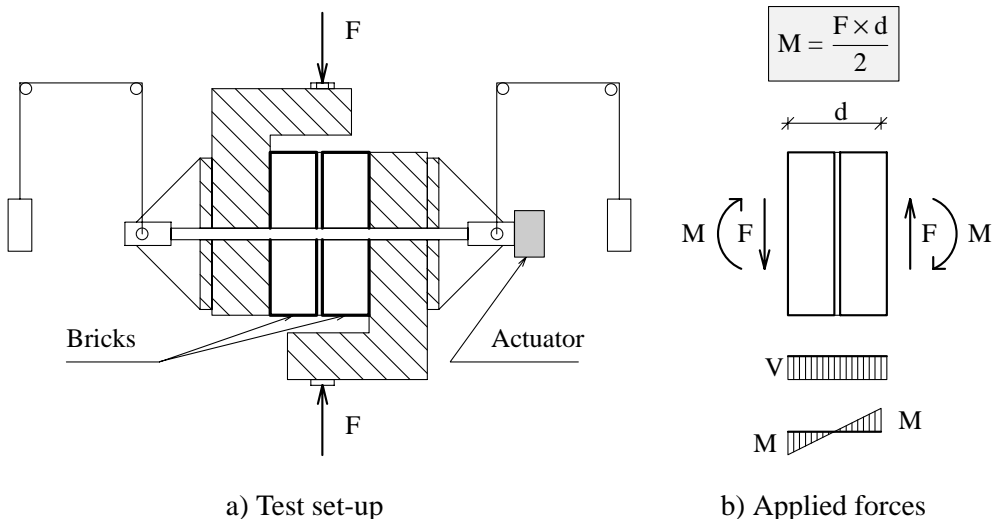


Fig. 4 - Apparatus to obtain shear behaviour (van der Pluijm 1992)

A discussion about the adequacy of the test set-up to generate an uniform state of stress in the sample will not be held here but the reader can find further references in van der Pluijm (1993) and Atkinson *et al.* (1989).

The experimental results yield an exponential shear softening curve (see Fig. 5) with a specimen value of the Mode II “fracture energy”, G_f^{II} , in the range 0.01-0.25 N/mm, according to the combination of unit and mortar. Here, G_f^{II} is the area defined by the $\tau-u_s$ curve and the residual dry friction shear level. Evaluation of the net bond surface of the specimens is no longer possible but the values measured previously can be assumed to hold. The value for the fracture energy depends also on the level of the confining stress (see Fig. 6). For the values of confining stresses tested the Coulomb friction yield surface seems to be suitable for the joint shear failure (Fig. 7) and the values of the cohesion c , the initial internal friction angle ϕ_0 , the ultimate internal friction angle ϕ_u and the dilatancy angle ψ can be directly measured. Values for these properties can be found in van der Pluijm (1992b). Note that the dilatancy angle depends on the level of the confining stress (see Fig. 8). For low confining pressures, the average value of $\tan \psi$ falls in the range 0.2-0.4, depending on the roughness of the brick surface. For high confining pressures, $\tan \psi$ decreases to zero. With increasing slip, $\tan \psi$ must also decrease to zero due to the regularization of the sheared surfaces.

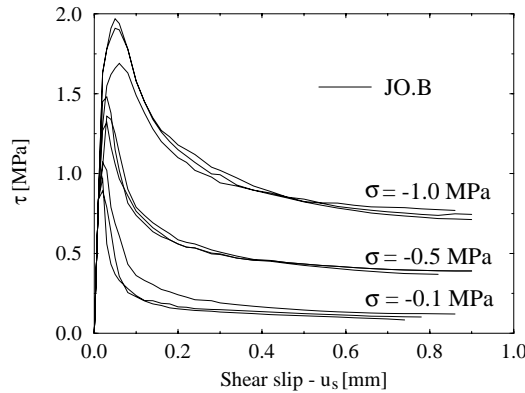


Fig. 5 - Stress-slip diagram

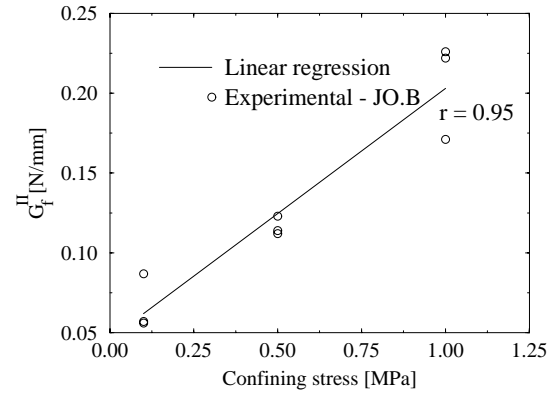
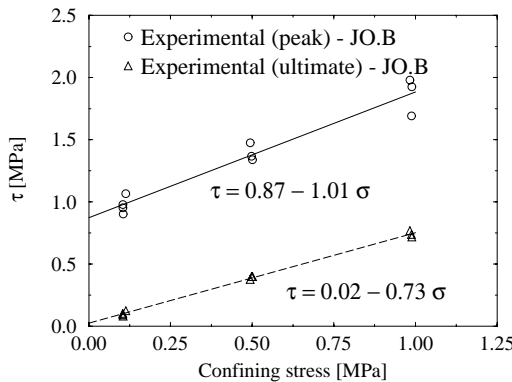
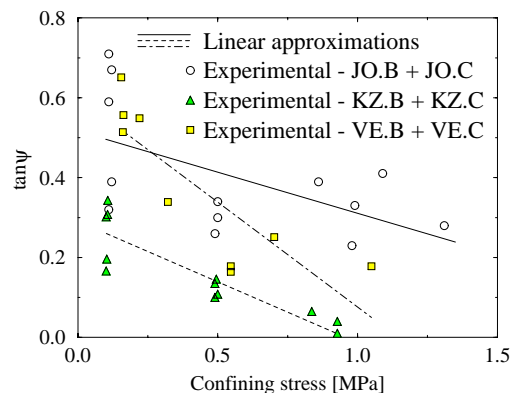
Fig. 6 - G_f^{II} vs. Confining stress

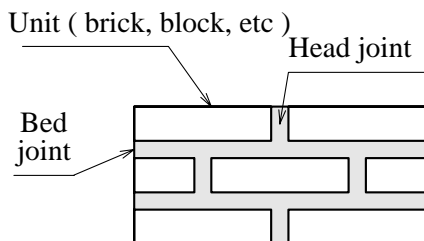
Fig. 7 - Yield surface calibration

Fig. 8 - $\tan \psi$ vs. Confining stress

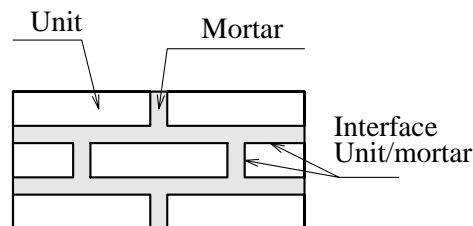
3. ABOUT A MODEL FOR THE ANALYSIS OF MASONRY STRUCTURES

In general, the approach towards modelling can focus on macro-modelling of masonry as a composite or micro-modelling of the individual components, viz. unit (brick, block, etc) and mortar, see also Rots (1991). The interface unit/mortar is responsible for most cracking as well as slip and can also be modelled. Along the present report the conjunction of mortar and interface unit/mortar will be referred to as joint. Depending on the level of accuracy and the simplicity desired, it is possible to use the following models (see Fig. 9):

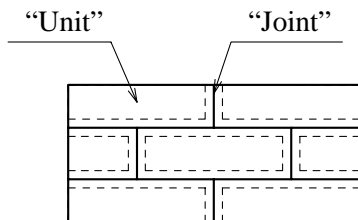
- Detailed micro-modelling - joints are represented by mortar continuum elements and discontinuum interface elements;
- Simplified micro-modelling - joints are represented by discontinuum elements;
- Macro-modelling - joints are smeared out in the continuum.



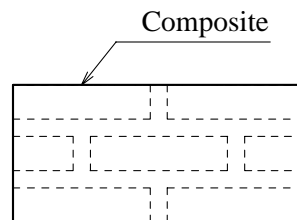
a) Masonry sample



b) Detailed micro-modelling



c) Simplified micro-modelling



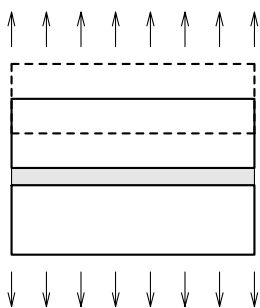
d) Macro-modelling

Fig. 9 - Modelling of masonry structures

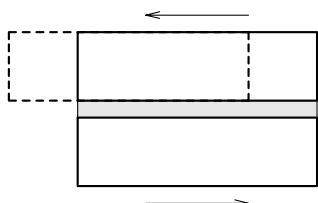
In the first approach, Young's modulus, Poisson's ratio and, optionally, inelastic properties of both unit and mortar are taken into account. The interface represents a potential crack/slippage plane with dummy stiffness to avoid interpenetration of the continuum. In the second approach, mortar is smeared out in the interface element and in the unit. Note that, due to the zero thickness of the interface elements, the geometry of the unit has to be expanded to include the thickness of the joint. In this approach the interface elastic stiffness has to be calculated taking into account the properties of both components. Accuracy is lost since Poisson's effect of the mortar is not included. The third approach does not make a distinction between individual units and joints but treats masonry as an anisotropic composite. The present report is focused in micro-modelling whereas macro-modelling will be reported later.

Regardless of the type of modelling adopted the following failure mechanisms, characteristic of masonry, must be considered (see Fig. 10):

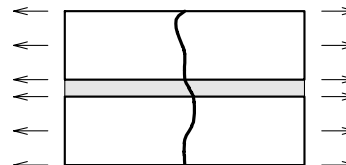
- (a) Cracking in the joints;
- (b) Sliding along bed or head joints at low values of normal stress;
- (c) Cracking of the units in direct tension;
- (d) Diagonal tension cracking of the units at values of normal stress sufficient to develop friction in joints;
- (e) Splitting of the units in tension as a result of mortar dilatancy at high values of normal stress.



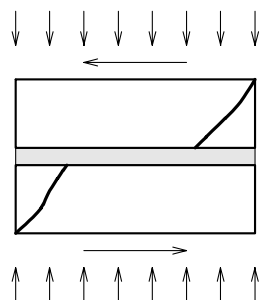
(a) Joint tension cracking



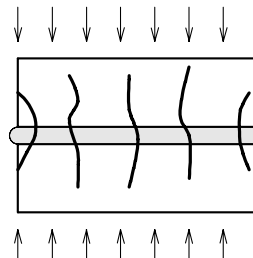
(b) Joint slip



(c) Unit direct tension crack



(d) Unit diagonal tension crack



(e) Masonry crushing

Fig. 10 - Failure mechanisms of masonry

3.1 Previous use of micro-modelling for masonry structures

Studies on micro-modelling applications are necessary to give deeper insight about the local behaviour of masonry structures. In fact, based only in composite modelling, it is difficult to extract information for use in typical building systems, unless the structure is composed of solid walls of sufficiently large dimensions so that the stresses across or along a macro-length will be essentially uniform. This of course cannot be the case with several building systems, particularly those made of concrete or calcium-silicate blocks, because window and door openings often result in piers that are only a few units in length. These piers are likely to determine the behaviour of the entire wall. Additionally, it is difficult to adequately respect masonry material constitutive laws with composite modelling and represent all the phenomena described in Fig. 10. Composite modelling is probably more practice oriented due to the facility of mesh generation, reduced time and memory exigences. This type of modelling is most valuable when a compromise between accuracy and efficiency is needed. Thus, both reliable micro- and macro-models need to be developed for the analysis of masonry structures.

Page (1978) made the first attempt to use a micro-model for masonry structures. This author modelled units as elastic continuum elements, bonded with interface elements. The elastic interface (σ, τ) – space was limited by the envelope obtained experimentally and shown in Fig. 11. Here σ is the joint normal stress and τ is the joint shear stress. The yield surface of Fig. 11 contains three different branches: one in tension and two in compression. The marked change in slope in compression corresponds to a change in the failure mode from pure shear failure in the joint to combined joint/unit failure.

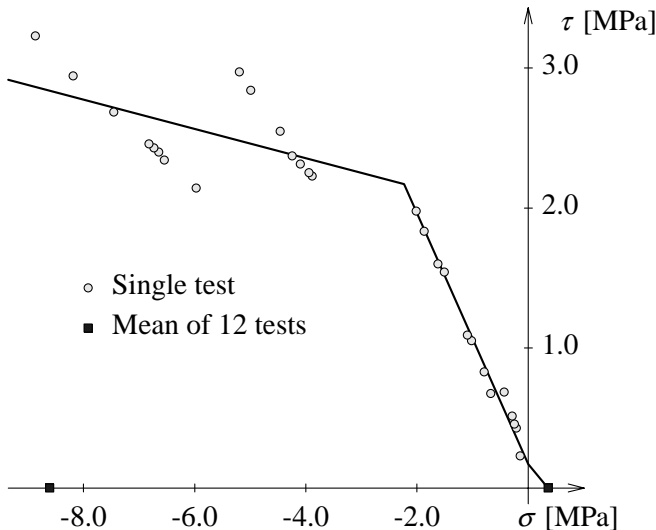


Fig. 11 - Interface failure envelope (Page 1978)

Non-linear behaviour included brittle failure in tension and hardening in shear/compression. Hardening was simulated in a primitive way, assuming that the normal stiffness remains constant and the shear stiffness follows an experimental curve. The adopted curve is, however, in opposition with recent experimental results (Atkinson *et al.* 1989, van der Pluijm 1992b) as softening is not considered. The model was able to reproduce the stress distributions in a bending test on a deep masonry beam under vertical load (see also Section 6). No load-displacement comparison between the model and the experiment is available and, as recognized by the author, an estimate of the ultimate

load is not possible because compressive failure is not included in the model. However, an attempt to include all the other masonry failure mechanisms was made and this work represented a most valuable improvement in masonry modelling.

Arya and Hegemier (1978) proposed a different model for grouted masonry. A von Mises strain softening model for compression with a tension cut-off was used for the units. Joints were modelled with interface elements with softening on both the cohesion and friction angle but a brittle tension cut-off. The collapse load obtained with this model shows good agreement with experimental results on shear walls but in the deformed meshes shown by these authors spurious modes are quite evident. The numerical procedures adopted to obtain a converged solution are also questionable.

To the knowledge of the authors posterior attempts to use interface elements - or springs - (Chiostriini *et al.* 1989, Saadeghvaziri and Metha 1993) or discrete elements (Dialer 1992, Vermeltfoort *et al.* 1993) for masonry structures do not represent significant improvements of the models described above. All these models include only tensile (brittle) and shear failure (brittle or elastic/ideal plastic) of the joint. Vermeltfoort *et al.* (1993) included also elastic/ideal plastic failure for the units but this is shown to be clearly insufficient (see also Fig. 52). No gradual softening behaviour after initiation of cracking or slip has been included in the models.

Some attempts on the use of detailed micro-models were also carried out, for example Ignatakis *et al.* (1989) and Riddington and Ghazali (1990). However this fine modelling can only be used for small specimens due to time and memory exigences and is not considered here. Instead a simplified micro-model is used. This model aims to model rationally softening, both in tension, shear and compression. An additional characteristic is that underlying parameters of the models have been measured directly from micro-experiments.

3.2 Adopted modelling strategy

In the simplified micro-model adopted here, units are modelled with continuum elements and joints are modelled with isoparametric interface elements. Interface elements allow discontinuities in the displacement field and establish a direct relation between tractions (σ , τ) and relative displacements across the interface (u_n , u_s). This relation is usually written as

$$\mathbf{t} = \mathbf{D} \mathbf{u}, \quad (1)$$

where $\mathbf{t} = (\sigma, \tau)^T$, $\mathbf{D} = \text{diag}(k_n, k_s)$ and $\mathbf{u} = (u_n, u_s)^T$. Here a plane stress configuration is assumed. The formulation of interface elements is fairly standard and will not be revised here. The reader is referred to Hohberg (1992) for an exhaustive discussion. One of the most important issues is the selection of an appropriate integration scheme as Gauss integration was reported to lead to oscillations of stresses when high dummy stiffnesses are used, see also Rots (1988) and Schellekens (1992).

The question remains of how to consider all phenomena in the model. The author tried before to model the failure of mortar in shear and tension in the joint with an interface model that included non-associated Coulomb friction with mode II softening on the cohesion c and a parabolic discrete cracking mode I softening on the tensile strength f_t (Lourenço and Rots 1992). Compressive crushing of masonry was modelled in the unit. In Lourenço and Rots (1992) this strategy was applied to the analysis of shear-walls and it was then concluded that modelling of cracks in the units might be necessary. Otherwise an overstiff post-peak response can be obtained, leading to a

limit load much higher than the one observed in the experiments (see also Section 7). Inclusion of a smeared crack approach for the units leads to numerical difficulties and, presently, does not seem to be a solution. The approach followed here is to concentrate all the damage in the relatively weak joints and, if necessary, in potential pure tension cracks in the units placed vertically in the middle of each unit (see Fig. 12). The joint interface yield surface has then to include all the mechanisms referred above except uniaxial tensile cracking of the unit. Inclusion of the first two mechanisms (tensile and shear failure of the joint) was shown to be quite standard but the proposal here set forth is novel. By limiting the compression/shear stress combinations the compressive damage can be included in the model as well as the combined mortar shear failure and unit diagonal tension failure. Therefore a compression cap will be added to standard models. The new interface cap model to be developed is used at a micro-level. Remarkably, experiments carried out in shear-walls (Mann and Müller 1982) and panels subjected to an uniform state of stress (Dialer 1991) result in similar macro-level yield surfaces (see Fig. 13).

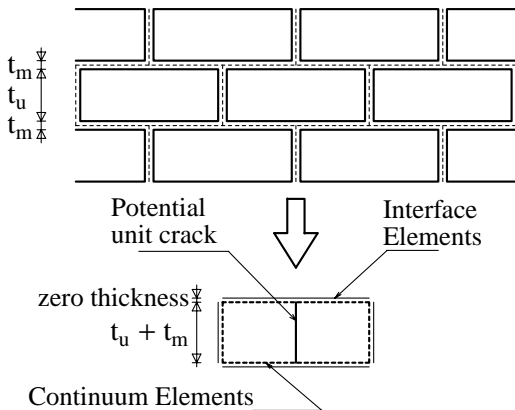


Fig. 12 - Suggested modelling strategy

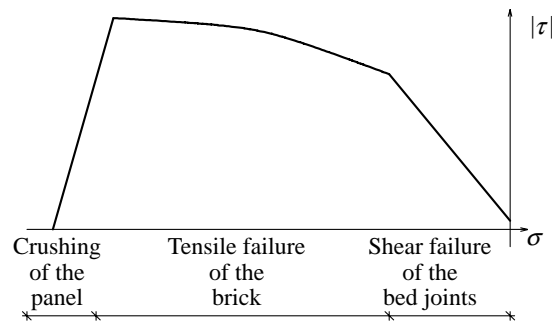


Fig. 13 - Failure surface (Mann and Müller 1982)

3.2.1 Assessment of the modelling strategy

We introduce now the quantities E_u , the Young's modulus of the unit, and E_m , the Young's modulus of the mortar. Fig. 12 shows that due to the zero thickness inherent in the interface element formulation the geometry of the units has to be expanded of the mortar thickness t_m in both x, y-directions. It follows that the elastic properties of the expanded "unit" and the interface "joint" must be corrected to yield similar results. Due to the relative dimensions of mortar and unit, it is assumed that the elastic properties of the unit remain unchanged. Fig. 14 shows a masonry sample subjected to an uniform normal stress, an unit cell made of two half units and one joint as well as the simplified modelling adopted for the cell. We further assume an uniform stress distribution both in the unit and in the mortar. Then, by making the deformation of the real and simplified cells equal, the normal stiffness of the interface joint reads

$$k_n = \frac{E_u E_m}{t_m(E_u - E_m)}. \quad (2)$$

Similarly for the shear component we assume

$$k_s = \frac{G_u G_m}{t_m(G_u - G_m)}. \quad (3)$$

Here G_u and G_m are the shear modulae, respectively, for unit and mortar.

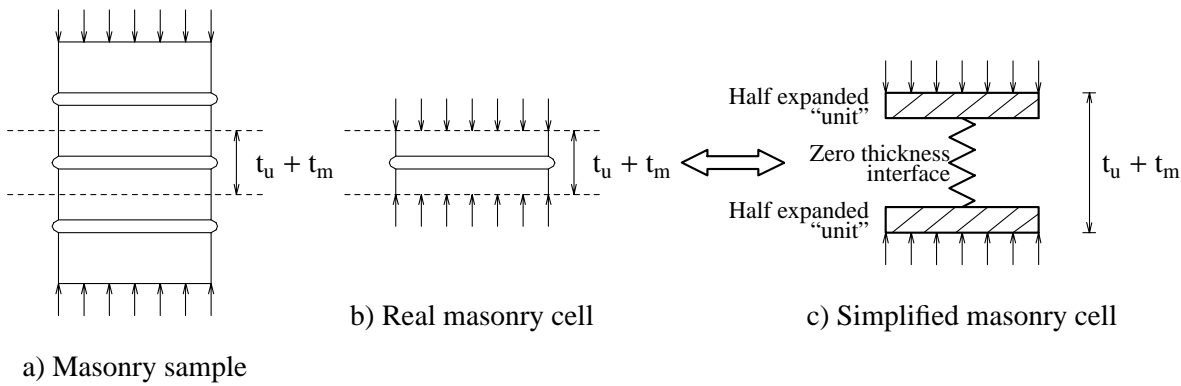


Fig. 14 - Calculation of the interface equivalent elastic stiffness

These formulae can be checked with a generic linear elastic calculation. A wall made of 18 layers of Joosten bricks ($52 \times 210 \times 100 \text{ mm}^3$) and a 10 mm mortar joint will be considered for this purpose. Two models are possible: Model 1, in which units and mortar are modelled with 8-noded continuum elements and Model 2, in which expanded “units” are modelled with 8-noded continuum elements and joints are modelled with 6-noded interface elements (see Fig. 15). The integration scheme used are 2×2 points Gauss integration for the continuum elements and 3 points Lobatto integration for the interface elements. The material properties used are given in Table 1.

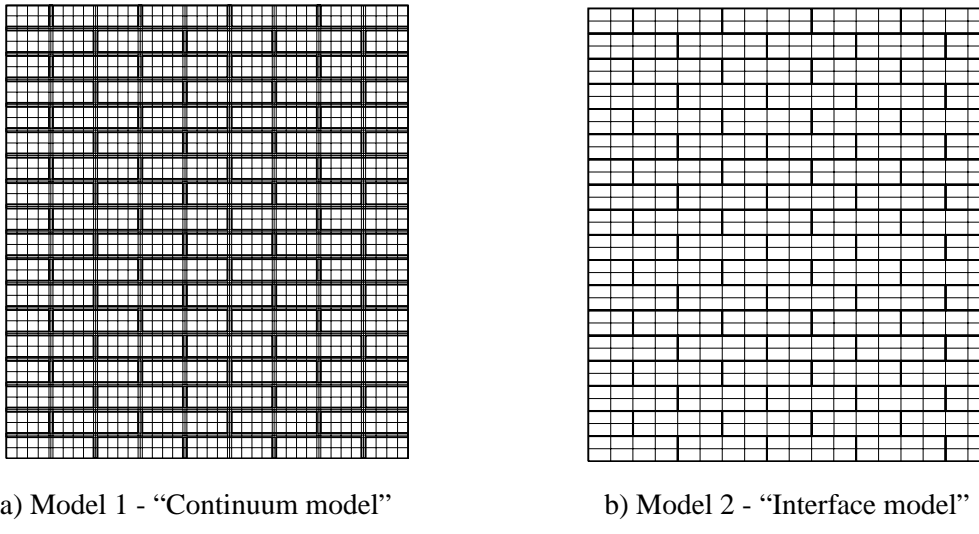


Fig. 15 - Models for masonry wall

Table 1 - Material properties

Continuum model		Interface model	
Unit	$E_u = 20000 \text{ N/mm}^2; \nu = 0.15$	“Unit”	$E_u = 20000 \text{ N/mm}^2; \nu = 0.15$
Mortar	$E_u = 2000 \text{ N/mm}^2; \nu = 0.125$	Joint	$k_n = 222 \text{ N/mm}^3; k_s = 99 \text{ N/mm}^3$

Four different loading are considered (see Fig. 16): two uniform loads along one edge and two point loads distributed over the right top unit. These loads (introduced by a displacement of 1.0 mm) as well as the parameters used to compare the performance of the two models are shown in Fig. 16.

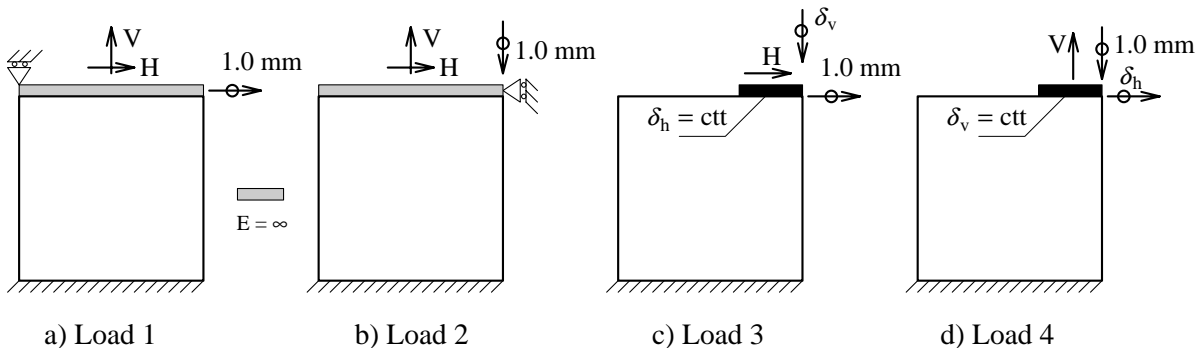


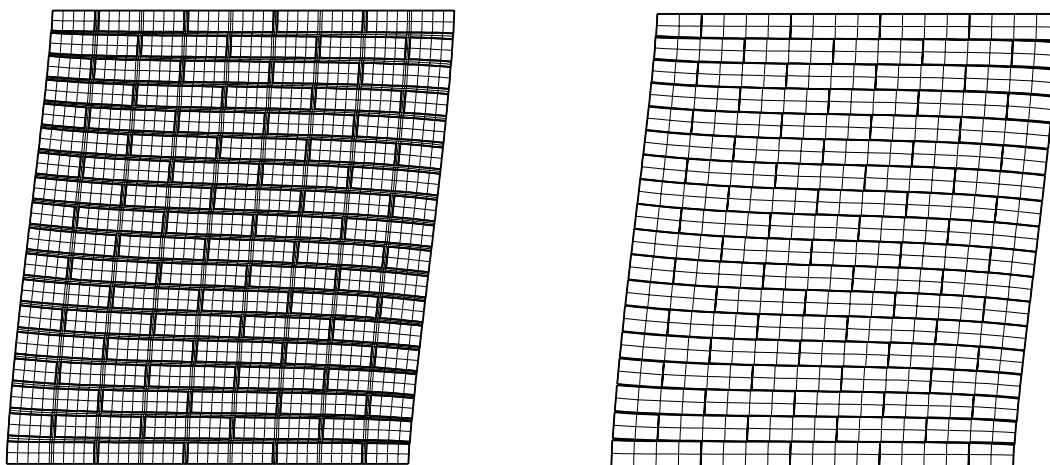
Fig. 16 - Loads applied to test masonry wall

In a Silicon Graphics Indigo R4400, on average, the continuum model used 333.5 sec of CPU time and the interface model 26.6 sec (8%). Table 2 gives the results obtained in a linear elastic calculation. The comparison results in a difference smaller than 2.5% between the two models.

Table 2 - Continuum vs. Interface modelling

	Continuum model				Interface model			
	H(kN)	V(kN)	δ_h (mm)	δ_v (mm)	H(kN)	V(kN)	δ_h (mm)	δ_v (mm)
Load 1	185.50	0.06	-	-	185.50	0.01	-	-
Load 2	-0.06	-739.50	-	-	-0.01	-752.80	-	-
Load 3	80.60	-	-	-0.4935	81.45	-	-	-0.4940
Load 4	-	-261.90	0.7592	-	-	-267.50	0.7522	-

The global behaviour of the simplified modelling shows excellent agreement with the global behaviour of the detailed modelling. Locally, however, some differences can be found and a detailed comparison will be given for the uniform loads. Figs. 17, 18 demonstrate that the deformational behaviour and the stress distribution for both modellings is similar. Note that Fig. 18 does not include the state of stress in the vertical joints and the stresses are shown at the level of the integration points of the interface model.

Fig. 17 - Deformed mesh for Load 1 ($\times 100$)

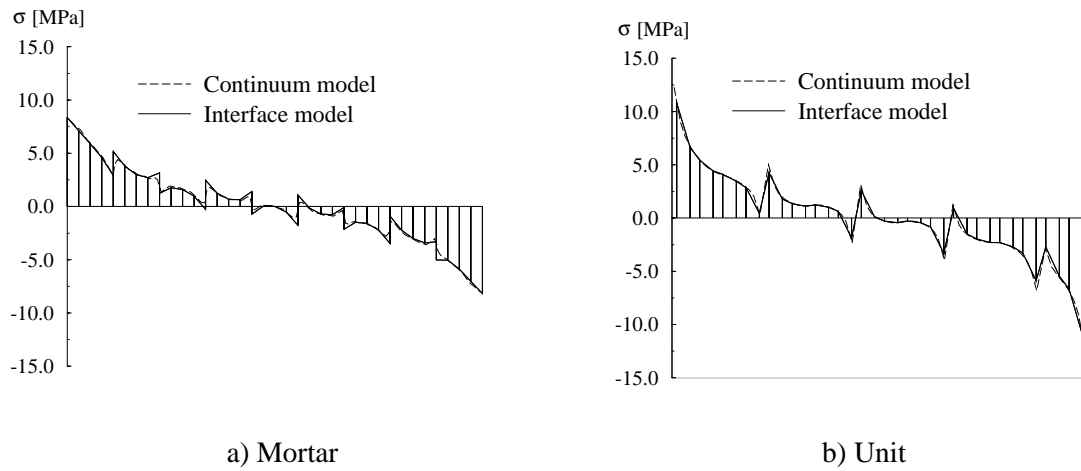


Fig. 18 - Vertical stresses at the base for Load 1

However, local stress gradients due to the different Young's modulae of the units and mortar can be averaged by the simplified model as shown in the detail of Fig. 19 for Load 2 (note that the results for the continuum model are obtained with a mesh refined by a factor 4). These local gradients are believed to be irrelevant for the global structural behaviour and are quickly smooth in presence of non-linear behaviour, see also Erkens (1994).

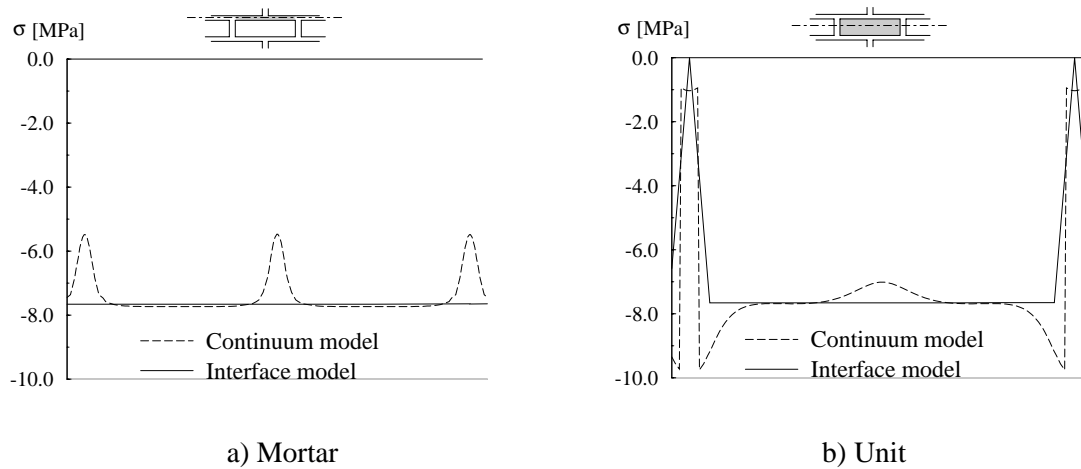


Fig. 19 - Vertical stresses at the center of the wall for Load 2

4. MULTISURFACE PLASTICITY

The interface behaviour is described in terms of a relation between the tractions \mathbf{t} and relative displacements \mathbf{u} across the interface. These quantities will be conveniently defined as $\boldsymbol{\sigma}$, generalized stress and $\boldsymbol{\varepsilon}$, generalized strain. In this case, eq. (1), the elastic constitutive relation between stresses and strains can be recast, in a usual fashion, as

$$\boldsymbol{\sigma} = \mathbf{D} \boldsymbol{\varepsilon}. \quad (4)$$

Here $\mathbf{D} = \text{diag}(k_n, k_s)$, $\boldsymbol{\sigma} = (\sigma, \tau)^T$ and $\boldsymbol{\varepsilon} = (u_n, u_s)^T$ for a 2D configuration. In the body of the present report only plane stress analysis will be considered but for the sake of completeness the changes necessary to a 3D configuration will be included in Appendix A.

The elastic domain is bounded by a composite yield surface that includes tension, shear and compression failure (see Fig. 20). For the implementation of this model single surface and multisurface plasticity theory is reviewed below in modern concepts, including consistent tangent operators and correct handling of the corners.

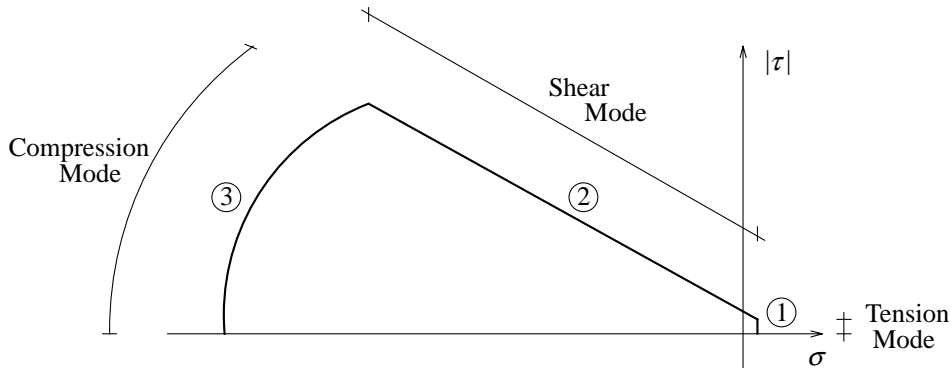


Fig. 20 - Composite yield surface

4.1 Elastoplastic equations

For multisurface plasticity the form of the elastic domain is defined by each yield function $f_i < 0$. Loading/unloading can be conveniently established in standard Kuhn-Tucker form by means of the conditions

$$\lambda_i \geq 0, f_i \leq 0 \text{ and } \lambda_i f_i = 0, \quad (5)$$

where λ_i is the plastic multiplier rate. Here it will be assumed that the yield functions are of the form

$$f_i(\boldsymbol{\sigma}, \kappa_i) = \Phi_i(\boldsymbol{\sigma}) + \Psi_i(\kappa_i) \quad (6)$$

where the scalar κ_i is introduced as a measure for the amount of hardening or softening and Φ_i , Ψ_i represent generic functions. For the case that the variables $\boldsymbol{\sigma}$ and κ_i are not separated refer to Appendix B. The usual elastoplastic equations for single surface plasticity hold: the total strain rate $\dot{\boldsymbol{\varepsilon}}$ is decomposed into an elastic component $\dot{\boldsymbol{\varepsilon}}^e$ and a plastic component $\dot{\boldsymbol{\varepsilon}}^p$

$$\dot{\boldsymbol{\varepsilon}} = \dot{\boldsymbol{\varepsilon}}^e + \dot{\boldsymbol{\varepsilon}}^p, \quad (7)$$

the elastic strain rate is related to the stress rate by the elastic constitutive matrix \mathbf{D} as

$$\dot{\boldsymbol{\sigma}} = \mathbf{D} \dot{\boldsymbol{\varepsilon}}^e \quad (8)$$

and the assumption of non-associated plasticity yields

$$\dot{\boldsymbol{\varepsilon}}^p = \lambda \frac{\partial g}{\partial \boldsymbol{\sigma}}, \quad (9)$$

where g is the plastic potential. The scalar λ introduced before reads, in case of strain hardening/softening,

$$\dot{\kappa} = \sqrt{(\dot{\boldsymbol{\varepsilon}}^p)^T \dot{\boldsymbol{\varepsilon}}^p} \quad (10a)$$

and, in the case of work hardening/softening,

$$\dot{\kappa} = \boldsymbol{\sigma}^T \dot{\boldsymbol{\varepsilon}}^p. \quad (10b)$$

For any corner of the proposed model two yield surfaces are active and the previous equations must be appropriately stated for multisurface plasticity. According to Koiter's generalization (Koiter 1953) eq. (9) reads

$$\dot{\boldsymbol{\varepsilon}}^p = \dot{\boldsymbol{\varepsilon}}_1^p + \dot{\boldsymbol{\varepsilon}}_2^p = \lambda_1 \frac{\partial g_1}{\partial \boldsymbol{\sigma}} + \lambda_2 \frac{\partial g_2}{\partial \boldsymbol{\sigma}}. \quad (11)$$

and, assuming a form of explicit coupling for the hardening/softening parameters, we obtain

$$\dot{\kappa}_1^{\text{corner}} = \dot{\kappa}_1 + \zeta_{12} \dot{\kappa}_2 \quad \text{and} \quad \dot{\kappa}_2^{\text{corner}} = \zeta_{21} \dot{\kappa}_1 + \dot{\kappa}_2, \quad (12)$$

where ζ_{12} and ζ_{21} are coupling terms. A form of implicit coupling can also be formulated upon substitution of eq. (11) in eq. (10) but, implicit coupling is complex to handle in the frame of a local Newton-Raphson solving scheme. Moreover, coupling cannot be controlled directly and will be present even when physically not acceptable. For these reasons explicit coupling is adopted here.

4.2 Integration of the elastoplastic equations

The return mapping algorithm is strain driven and basically consists of two steps, the calculation of the elastic trial stress, also called the elastic predictor, and the return mapping to the yield surface, i.e., the plastic corrector. We will use the implicit Euler backward integration scheme due to its unconditionally stability (Ortiz and Popov 1985) and accuracy (de Borst and Feenstra 1990). For single surface plasticity, manipulation of eqs. (7-9) for finite increments and application of an implicit Euler backward integration scheme give the update of the stress values as

$$\boldsymbol{\sigma}_{n+1} = \boldsymbol{\sigma}_n + \Delta \boldsymbol{\sigma}_{n+1} = \boldsymbol{\sigma}_n + \mathbf{D} \Delta \boldsymbol{\varepsilon}_{n+1}^e = \boldsymbol{\sigma}_n + \mathbf{D} (\Delta \boldsymbol{\varepsilon}_{n+1} - \Delta \boldsymbol{\varepsilon}_{n+1}^p). \quad (13)$$

This equation can be recast as

$$\boldsymbol{\sigma}_{n+1} = \boldsymbol{\sigma}_{n+1}^{\text{trial}} - \Delta \lambda_{n+1} \mathbf{D} \left. \frac{\partial g}{\partial \boldsymbol{\sigma}} \right|_{n+1} \quad (14)$$

with $\boldsymbol{\sigma}_{n+1}^{\text{trial}} = \boldsymbol{\sigma}_n + \mathbf{D} \Delta \boldsymbol{\varepsilon}_{n+1}$. The subscript $n+1$ means that all the quantities are evaluated at the final stage. For simplicity it will be, in general, dropped in the derivatives. Eq. (14) represents a non-linear system of equations with the stress tensor components and one scalar (usually $\Delta \lambda_{n+1}$) as unknowns. Enforcing the satisfaction of the yield condition at the final converged stage results in

the necessary additional equation:

$$f_{n+1} = 0. \quad (15)$$

The constitutive non-linear eqs. (14,15) at the integration point level can be solved locally with a regular Newton-Raphson method. In case that the necessary Jacobian is particularly difficult to calculate or quite cumbersome expressions are found, the initial Jacobian can be calculated numerically and updated with the Broyden's method, see Dennis and Schnabel (1983). In most cases, and for the yield functions used in this report, eq. (14) can be solved in order to obtain explicitly the updated stress value as a function of the updated plastic multiplier,

$$\boldsymbol{\sigma}_{n+1} = \boldsymbol{\sigma}_{n+1}(\Delta\lambda_{n+1}). \quad (16)$$

Furthermore, inserting eq. (9) in eq. (10) yields for finite increments

$$\Delta\kappa_{n+1} = \Delta\kappa_{n+1}(\boldsymbol{\sigma}_{n+1}, \Delta\lambda_{n+1}). \quad (17)$$

Substitution of these two equations in the yield function, cf. eq. (15), leads to a non-linear equation in one variable, namely $\Delta\lambda_{n+1}$: $f_{n+1}(\Delta\lambda_{n+1}) = 0$. This constitutive equation is solved here with a local Newton method. The derivative of $f_{n+1}(\Delta\lambda_{n+1})$ with respect to $\Delta\lambda_{n+1}$, which is needed in this procedure, reads after some manipulation

$$\frac{\partial f}{\partial \Delta\lambda} \Bigg|_{n+1} = \boldsymbol{\gamma}^T \frac{\partial \boldsymbol{\sigma}}{\partial \Delta\lambda} - h, \quad (18)$$

where the modified yield surface gradient $\boldsymbol{\gamma}$ and the hardening modulus h are given by

$$\boldsymbol{\gamma} = \frac{\partial f}{\partial \boldsymbol{\sigma}} + \frac{\partial f}{\partial \kappa} \frac{\partial \kappa}{\partial \boldsymbol{\sigma}} \Bigg|_{n+1} \quad \text{and} \quad h = -\frac{\partial f}{\partial \kappa} \frac{\partial \kappa}{\partial \Delta\lambda} \Bigg|_{n+1}. \quad (19)$$

As referred above, if this derivative is particularly difficult to obtain, a secant method can be used to approximate the exact derivative. In this case, an estimate of the initial value of $\Delta\lambda_{n+1}$ is necessary. A series expansion of the yield surface around the trial stress gives

$$f_{n+1} \approx f_{n+1}^{\text{trial}} + \left(\frac{\partial f}{\partial \boldsymbol{\sigma}} \right)_{\text{trial}}^T \Delta\boldsymbol{\sigma}_{n+1} + \left(\frac{\partial f}{\partial \kappa} \right)_{\text{trial}} \Delta\kappa_{n+1} = 0 \quad (20)$$

and, after some algebra, the initial estimate for $\Delta\lambda_{n+1}$ reads

$$\Delta\lambda_{n+1}^{(0)} = \frac{f_{n+1}^{\text{trial}}}{h + \left(\frac{\partial f}{\partial \boldsymbol{\sigma}} \right)^T \mathbf{D} \frac{\partial g}{\partial \boldsymbol{\sigma}}}, \quad (21)$$

where all the quantities are evaluated at the trial state. Note that to obtain this expression for $\Delta\lambda_{n+1}^{(0)}$ eqs. (8,9) are used in the incremental form, with $\Delta\boldsymbol{\epsilon} = 0$ because the total strain has already been applied to calculate the trial stress.

For multisurface plasticity a similar procedure applies and eq. (14) reads now

$$\boldsymbol{\sigma}_{n+1} = \boldsymbol{\sigma}_{n+1}^{\text{trial}} - \Delta\lambda_{1, n+1} \mathbf{D} \frac{\partial g_1}{\partial \boldsymbol{\sigma}} \Bigg|_{n+1} - \Delta\lambda_{2, n+1} \mathbf{D} \frac{\partial g_2}{\partial \boldsymbol{\sigma}} \Bigg|_{n+1}. \quad (22)$$

We shall equally assume that this equation can be solved explicitly as

$$\boldsymbol{\sigma}_{n+1} = \boldsymbol{\sigma}_{n+1}(\Delta\lambda_{1, n+1}, \Delta\lambda_{2, n+1}). \quad (23)$$

As for single surface plasticity, eqs. (12) yield for finite increments

$$\begin{cases} \kappa_{1, n+1}^{\text{corner}} = \kappa_{1, n+1}^{\text{corner}}(\boldsymbol{\sigma}_{n+1}, \Delta\lambda_{1, n+1}, \Delta\lambda_{2, n+1}) \\ \kappa_{2, n+1}^{\text{corner}} = \kappa_{2, n+1}^{\text{corner}}(\boldsymbol{\sigma}_{n+1}, \Delta\lambda_{1, n+1}, \Delta\lambda_{2, n+1}) \end{cases}. \quad (24)$$

Substitution of these two equations in the active yield functions leads to a non-linear system of equations with a set of scalar unknowns, namely $\Delta\lambda_{1, n+1}$ and $\Delta\lambda_{2, n+1}$:

$$\begin{cases} f_{1, n+1}(\Delta\lambda_{1, n+1}, \Delta\lambda_{2, n+1}) = 0 \\ f_{2, n+1}(\Delta\lambda_{1, n+1}, \Delta\lambda_{2, n+1}) = 0 \end{cases}. \quad (25)$$

This non-linear constitutive system of equations is solved by a local Newton-Raphson iterative method. The Jacobian necessary for the Newton-Raphson scheme reads

$$\mathbf{J}_{n+1} = \begin{bmatrix} \boldsymbol{\gamma}_1^T \frac{\partial \boldsymbol{\sigma}}{\partial \Delta\lambda_1} - h_1 & | & \boldsymbol{\gamma}_1^T \frac{\partial \boldsymbol{\sigma}}{\partial \Delta\lambda_2} + \frac{\partial f_1}{\partial \kappa_1} \frac{\partial \kappa_1}{\partial \Delta\lambda_2} \\ \hline \boldsymbol{\gamma}_2^T \frac{\partial \boldsymbol{\sigma}}{\partial \Delta\lambda_1} + \frac{\partial f_2}{\partial \kappa_2} \frac{\partial \kappa_2}{\partial \Delta\lambda_1} & | & \boldsymbol{\gamma}_2^T \frac{\partial \boldsymbol{\sigma}}{\partial \Delta\lambda_1} - h_2 \end{bmatrix}. \quad (26)$$

where

$$\boldsymbol{\gamma}_i = \frac{\partial f_i}{\partial \boldsymbol{\sigma}} + \frac{\partial f_i}{\partial \kappa_i} \frac{\partial \kappa_i}{\partial \boldsymbol{\sigma}} \Bigg|_{n+1} \quad \text{and} \quad h_i = -\frac{\partial f_i}{\partial \kappa_i} \frac{\partial \kappa_i}{\partial \Delta\lambda_i} \Bigg|_{n+1}. \quad (27)$$

As before, if a secant (Broyden's) method is used instead to solve the local return mapping system of equations, an initial estimate of the values of $\Delta\lambda_{n+1}^i$ is necessary. This can be easily done by a series expansion of the yield surfaces around the trial stress.

The problem that remains is how to determine the set of active yield functions. Simo *et al.* (1988b) introduced firstly consistent numerical algorithms for multisurface plasticity. These authors proved that under certain assumptions for the hardening law (which includes ideal plasticity and does not necessarily preclude softening) the number of active yield functions is less or equal than the number of possible active yield functions (defined by $f_i^{\text{trial}} \geq 0$). Under this assumption two numerical procedures for the return mapping are put forward:

1. Assume that all possible active yield surfaces are active and solve the return mapping. Check the sign of all $\Delta\lambda_{n+1}^i$. If any $\Delta\lambda_{n+1}^i < 0$ drop this yield function and restart, otherwise exit.
2. In the previous procedure the number of active yield functions remains unchanged during the iterative process to obtain the solution. In the second procedure the number of active yield functions is allowed to change during the iterative process as follows:
 - Iterate to solve the return mapping. For iteration j the value of the plastic multipliers is $(\Delta\lambda_{n+1}^i)_j$;
 - If any $(\Delta\lambda_{n+1}^i)_j < 0$ then remove this yield function and restart the iteration with the new set of yield functions, otherwise proceed to the next iteration.

Procedure 2 can only be applied if all $\Delta\lambda_{n+1}^i$ can be shown to remain positive during the iterative process. This is very limitative, even in the case of hardening plasticity when the plastic multiplier of a particular yield function can increase monotonically from negative to positive values. Already Pramono and William (1989) questioned these procedures advocating that the trial value of the yield functions cannot provide a sufficient criterion for determining which surface is active near a singular region.

Feenstra (1993) suggests a quite elegant and efficient computational implementation, best suitable when the number of yield functions is small. The system of non-linear equations, eqs. (25), is substituted by

$$\begin{cases} c_1 f_{1,n+1}(\Delta\lambda_{1,n+1}, \Delta\lambda_{2,n+1}) = 0 \\ c_2 f_{2,n+1}(\Delta\lambda_{1,n+1}, \Delta\lambda_{2,n+1}) = 0 \end{cases}, \quad (28)$$

where c_i represents a set of unitary constants that are set to zero if in iteration j the correspondent $(\Delta\lambda_{n+1}^i)_j$ is negative. The update of the Jacobian is made with Broyden's method, see Dennis and Schnabel (1983). This procedure is particularly interesting as there is no need to change the Jacobian according to the number of current active yield surfaces. One problem that remains is the calculation of the initial Jacobian approximated by this author from the linearization of both yield surfaces in the trial state, assuming implicitly that all the yield functions are active. Unfortunately this procedure does not guarantee that the updated Jacobian will converge to the exact Jacobian with the inherent risks of divergency and poor rate of convergence. None of those problems were reported by Feenstra (1993). However, in section 5 of this report it is shown that, for the implemented cap model, the Broyden's method can fail to converge in case of large steps and strong non-linearities.

In the present report a trial and error procedure to solve the return mapping is used aiming at a robust and always convergent algorithm. It will be assumed that the set of initial active yield functions is the one defined by Simo *et al.* (1988b) ($f_i^{\text{trial}} \geq 0$). If, after the return mapping is completed, any $\Delta\lambda_{n+1}^i < 0$ or $f_{n+1}^i > 0$ is found, the number of active yield surfaces is adjusted accordingly and the return mapping is restarted. In general, this process can lead to one unsuccessful return mapping but, rarely and only for larger increments, to more unsuccessful return mappings before the correct number of active yield surfaces is obtained (see Fig. 21). Note that in this figure, for simplicity, the yield surface at the stage $n+1$ corresponding to the return mapping of different modes was assumed to coincide.

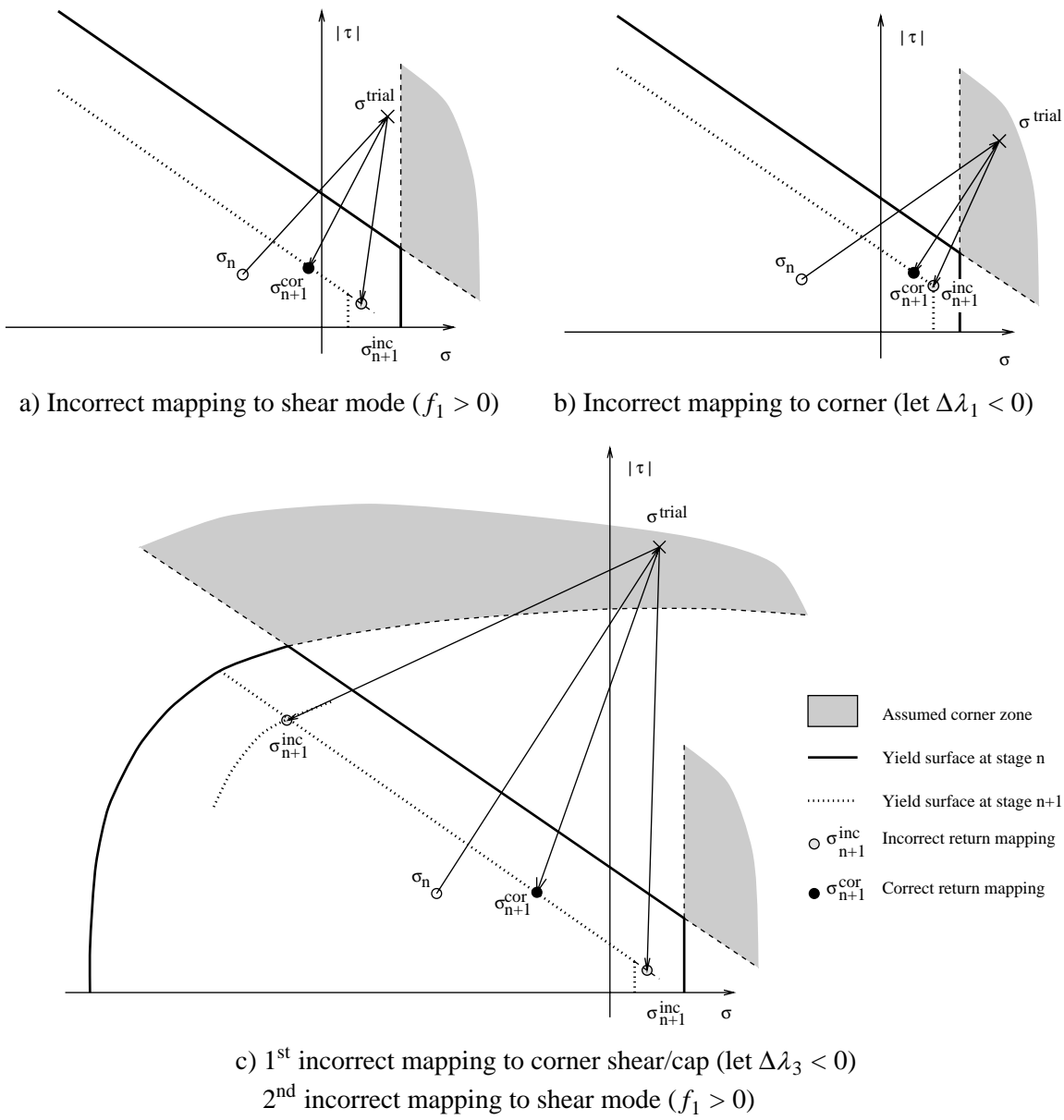


Fig. 21 - Example of possible initial unsuccessful return mappings

4.3 Evaluation of the tangent operator

A tangent operator consistent with the integration algorithm is needed to obtain quadratic convergence and a robust global Newton-Raphson method. Its expression can be easily derived from the update equations and the consistency condition ($d f_{n+1} = 0$). For single surface plasticity, differentiation of the update equations, eqs. (14,17), yields

$$d\boldsymbol{\sigma}_{n+1} = \mathbf{H}^{-1} \left(d\boldsymbol{\varepsilon}_{n+1} - d\lambda_{n+1} \frac{\partial g}{\partial \boldsymbol{\sigma}} \right) \quad (29)$$

$$d\boldsymbol{\kappa}_{n+1} = \left(\frac{\partial \boldsymbol{\kappa}}{\partial \boldsymbol{\sigma}} \right)^T d\boldsymbol{\sigma}_{n+1} + \frac{\partial \boldsymbol{\kappa}}{\partial \Delta \lambda} d\lambda_{n+1} \quad (30)$$

and the consistency condition reads

$$df_{n+1} = \left(\frac{\partial f}{\partial \boldsymbol{\sigma}} \right)^T d\boldsymbol{\sigma}_{n+1} + \frac{\partial f}{\partial \kappa} d\kappa_{n+1} = 0 , \quad (31)$$

where the modified compliance matrix \mathbf{H} is given by

$$\mathbf{H} = \mathbf{D}^{-1} + \Delta\lambda_{n+1} \frac{\partial^2 g}{\partial \boldsymbol{\sigma}^2} \quad (32)$$

Upon substitution of eqs. (29,30) in eq. (31) we obtain

$$d\lambda_{n+1} = \frac{\boldsymbol{\gamma}^T \mathbf{H}^{-1}}{h + \boldsymbol{\gamma}^T \mathbf{H}^{-1} \frac{\partial g}{\partial \boldsymbol{\sigma}}} d\boldsymbol{\epsilon}_{n+1} \quad (33)$$

and further substitution of this value in eq. (29) yields, finally, the consistent tangent operator \mathbf{D}^{ep} as

$$\mathbf{D}^{ep} = \frac{d\boldsymbol{\sigma}}{d\boldsymbol{\epsilon}} \Big|_{n+1} = \mathbf{H}^{-1} - \frac{\mathbf{H}^{-1} \frac{\partial g}{\partial \boldsymbol{\sigma}} \boldsymbol{\gamma}^T \mathbf{H}^{-1}}{h + \boldsymbol{\gamma}^T \mathbf{H}^{-1} \frac{\partial g}{\partial \boldsymbol{\sigma}}} \quad (34)$$

Note that the modified yield surface gradient $\boldsymbol{\gamma}$ and the hardening modulus h were defined in eq. (19).

This expression for \mathbf{D}^{ep} is particularly interesting as it clearly shows that a non-symmetric tangent operator will be obtained even in the case of associated plasticity if the hardening parameter update is not a linear function of the plastic multiplier update, i.e., if $\Delta\kappa_{n+1} \neq c\Delta\lambda_{n+1}$, where c is a constant.

Similarly, for multisurface plasticity a tangent operator consistent with the integration algorithm can be obtained from the update equations and the consistent conditions ($df_{1,n+1} = 0$ and $df_{2,n+1} = 0$). Differentiation of the update equations, eqs. (22,24), yields

$$d\boldsymbol{\sigma}_{n+1} = \mathbf{H}^{-1} \left(d\boldsymbol{\epsilon}_{n+1} - d\lambda_{1,n+1} \frac{\partial g_1}{\partial \boldsymbol{\sigma}} - d\lambda_{2,n+1} \frac{\partial g_2}{\partial \boldsymbol{\sigma}} \right) \quad (35)$$

$$d\kappa_{1,n+1} = \left(\frac{\partial \kappa_1}{\partial \boldsymbol{\sigma}} \right)^T d\boldsymbol{\sigma}_{n+1} + \frac{\partial \kappa_1}{\partial \Delta\lambda_1} d\lambda_{1,n+1} + \frac{\partial \kappa_1}{\partial \Delta\lambda_2} d\lambda_{2,n+1} \quad (36)$$

$$d\kappa_{2,n+1} = \left(\frac{\partial \kappa_2}{\partial \boldsymbol{\sigma}} \right)^T d\boldsymbol{\sigma}_{n+1} + \frac{\partial \kappa_2}{\partial \Delta\lambda_1} d\lambda_{1,n+1} + \frac{\partial \kappa_2}{\partial \Delta\lambda_2} d\lambda_{2,n+1} \quad (37)$$

and the consistency condition reads

$$\begin{aligned} df_{1,n+1} &= \left(\frac{\partial f_1}{\partial \boldsymbol{\sigma}} \right)^T d\boldsymbol{\sigma}_{n+1} + \frac{\partial f_1}{\partial \kappa_1} d\kappa_{1,n+1} = 0 \\ df_{2,n+1} &= \left(\frac{\partial f_2}{\partial \boldsymbol{\sigma}} \right)^T d\boldsymbol{\sigma}_{n+1} + \frac{\partial f_2}{\partial \kappa_2} d\kappa_{2,n+1} = 0 \end{aligned} , \quad (38)$$

where the modified compliance matrix \mathbf{H} reads now

$$\mathbf{H} = \mathbf{D}^{-1} + \Delta\lambda_{1,n+1} \frac{\partial^2 g_1}{\partial \boldsymbol{\sigma}^2} + \Delta\lambda_{2,n+1} \frac{\partial^2 g_2}{\partial \boldsymbol{\sigma}^2} . \quad (39)$$

Upon substitution of eqs. (35-37) in eqs. (38) we obtain

$$\begin{Bmatrix} d\lambda_{1,n+1} \\ d\lambda_{2,n+1} \end{Bmatrix} = \mathbf{A}^{-1} \begin{Bmatrix} \boldsymbol{\gamma}_1^T \mathbf{H}^{-1} d\boldsymbol{\epsilon}_{n+1} \\ \boldsymbol{\gamma}_2^T \mathbf{H}^{-1} d\boldsymbol{\epsilon}_{n+1} \end{Bmatrix} \quad (40)$$

where the matrix \mathbf{A} reads

$$\mathbf{A} = \begin{bmatrix} \boldsymbol{\gamma}_1^T \mathbf{H}^{-1} \frac{\partial g_1}{\partial \boldsymbol{\sigma}} + h_1 & | & \boldsymbol{\gamma}_1^T \mathbf{H}^{-1} \frac{\partial g_2}{\partial \boldsymbol{\sigma}} - \frac{\partial f_1}{\partial \kappa_1} \frac{\partial \kappa_1}{\partial \Delta \lambda_2} \\ \hline \boldsymbol{\gamma}_2^T \mathbf{H}^{-1} \frac{\partial g_1}{\partial \boldsymbol{\sigma}} - \frac{\partial f_2}{\partial \kappa_2} \frac{\partial \kappa_2}{\partial \Delta \lambda_1} & | & \boldsymbol{\gamma}_2^T \mathbf{H}^{-1} \frac{\partial g_2}{\partial \boldsymbol{\sigma}} + h_2 \end{bmatrix}. \quad (41)$$

Further substitution of $d\lambda_{1,n+1}$ and $d\lambda_{2,n+1}$ in eq. (35) yields the expression of the consistent tangent operator \mathbf{D}^{ep} as

$$\mathbf{D}^{ep} = \frac{d\boldsymbol{\sigma}}{d\boldsymbol{\varepsilon}} \Big|_{n+1} = \mathbf{H}^{-1} - \mathbf{H}^{-1} \left(\sum_{i=1}^{i=2} \sum_{j=1}^{j=2} a_{ij}^{-1} \frac{\partial g_i}{\partial \boldsymbol{\sigma}} \boldsymbol{\gamma}_j^T \right) \mathbf{H}^{-1} \quad (42)$$

where a_{ij}^{-1} are the coefficients of \mathbf{A}^{-1} . Note that the modified yield surface gradient $\boldsymbol{\gamma}_i$ and the hardening modulus h_i were defined in eq. (27).

The expression for the consistent tangent operator for multisurface plasticity can be also written in a matrix form following Riggs and Powel (1990). Substitution of eqs. (36,37) in eq. (38) yields

$$\mathbf{E} d\boldsymbol{\lambda}_{n+1} = \mathbf{V}^T d\boldsymbol{\sigma}_{n+1}, \quad (43)$$

where the vector $d\boldsymbol{\lambda}_{n+1}$ reads

$$d\boldsymbol{\lambda}_{n+1} = \left\{ d\lambda_{1,n+1}, d\lambda_{2,n+1} \right\}^T, \quad (44)$$

the matrix \mathbf{V} reads

$$\mathbf{V} = \begin{bmatrix} \boldsymbol{\gamma}_1 & \boldsymbol{\gamma}_2 \end{bmatrix} \quad (45)$$

and the matrix \mathbf{E} reads

$$\mathbf{E} = \begin{bmatrix} -h_1 & | & \frac{\partial f_1}{\partial \kappa_1} \frac{\partial \kappa_1}{\partial \Delta \lambda_2} \\ \hline \frac{\partial f_2}{\partial \kappa_2} \frac{\partial \kappa_2}{\partial \Delta \lambda_1} & | & -h_2 \end{bmatrix}. \quad (46)$$

Eq. (35) can be recast as

$$d\boldsymbol{\sigma}_{n+1} = \mathbf{H}^{-1} (d\boldsymbol{\varepsilon}_{n+1} - \mathbf{U} d\boldsymbol{\lambda}_{n+1}), \quad (47)$$

where the matrix \mathbf{U} reads

$$\mathbf{U} = \begin{bmatrix} \frac{\partial g_1}{\partial \boldsymbol{\sigma}} & \frac{\partial g_2}{\partial \boldsymbol{\sigma}} \end{bmatrix}. \quad (48)$$

Upon substitution of eq. (47) in eq. (43) we obtain

$$d\lambda_{n+1} = \left(\mathbf{E} + \mathbf{V}^T \mathbf{H}^{-1} \mathbf{U} \right)^{-1} \mathbf{V}^T \mathbf{H}^{-1} d\boldsymbol{\varepsilon}_{n+1} \quad (49)$$

and further substitution of this value in eq. (47) yields, finally, the consistent tangent operator \mathbf{D}^{ep} as

$$\mathbf{D}^{ep} = \frac{d\boldsymbol{\sigma}}{d\boldsymbol{\varepsilon}} \Bigg|_{n+1} = \mathbf{H}^{-1} - \mathbf{H}^{-1} \mathbf{U} \left(\mathbf{E} + \mathbf{V}^T \mathbf{H}^{-1} \mathbf{U} \right)^{-1} \mathbf{V}^T \mathbf{H}^{-1}. \quad (50)$$

5. REFERENCES

- Arya, S.K., Hegemier, G.A., On non-linear response predictions of concrete masonry assemblies, Proc. North American Masonry Conf., pp. 19.1-19.24 (1978)
- Atkinson, R.H., Amadei, B.P., Saeb, S. and Sture, S., Response of masonry bed joints in direct shear, *J. Struc. Engrg.*, ASCE, Vol. 115(9), pp. 2276-2296 (1989)
- Atkinson, R.H. and Yan, G.G., Results of a statistical study of masonry deformability, *The Masonry Society Journal*, Vol. 9(1), pp. 81-90 (1990)
- Bierwirth, H., Stöckl, S. and Kupfer, H., Triaxial tests on mortar specimens taken from bed joints, Proc. 6th North American Masonry Conf., Philadelphia, U.S.A., pp. 995-1007 (1993)
- de Borst, R. and Feenstra P.H., Studies in anisotropic plasticity with reference to the Hill criterion, *Int. J. Numer. Methods Engrg.*, Vol. 29, pp. 315-336 (1990)
- Chiostrini, S., Foraboschi, P. and Sorace, S., Problems connected with the arrangement of a non-linear finite element method to the analysis of masonry structures, in *Structural Repair and Maintenance of Historical Buildings*, Computational Mechanics Publications, pp. 525-534 (1989)
- Dennis, J.E. and Schnabel, R.B., *Numerical methods for unconstrained optimization and non-linear equations*, Prentice-Hall, Englewood Cliffs, New Jersey, U.S.A. (1983)
- Dialer, C., Some remarks on the strength and deformation behaviour of shear stressed masonry panels under static monotonic loading, Proc. 9th Int. Brick/Block Masonry Conf., Berlin, Germany, pp. 276-283 (1991)
- Dialer, C., A distinct element approach for the deformation behaviour of shear stressed masonry panels, Proc. 6th Canadian Masonry Symp., Saskatoon, Canada, pp. 765-776 (1992)
- DiMaggio, F.L. and Sandler, I.V., Material model for granular soils, *J. Engrg. Mech. Div.*, ASCE, Vol. 97(3), pp. 935-950 (1971)
- Drucker, D.C., Gibson, R.E. and Henkel, D.J., Soil mechanics and work hardening theories of plasticity, *Transactions of the ASCE*, Vol. 122, pp. 338-346 (1957)
- Drysdale, R.G. and Wong, H.E., Interpretation of the compressive strength of masonry prisms, Proc. 7th Int. Brick/Block Masonry Conf., Australia, pp. 617-624 (1985)
- Erkens, S., Numerical research on cracking of masonry under restrained shrinkage, Graduation report of Delft University of Technology, report 94-CON-R0376, TNO/TU Delft, Building and Construction Research, The Netherlands (in Dutch) (1994)
- Feenstra, P.H., Computational aspects of biaxial stress in plain and reinforced concrete, Dissertation, Delft University of Technology, Delft, The Netherlands (1993)
- Hoek, E., Strength of jointed rock masses, *Géotechnique*, Vol. 33(3), pp. 187-223 (1983)
- Hohberg, J.-M., A joint element for the nonlinear dynamic analysis of arch dams, Report No. 186, Institute of Structural Engineering, ETH Zurich, Switzerland (1992)
- Hofstetter, G., Simo, J.C. and Taylor, R.L., A modified cap model: closest point solution algorithms, *Computers & Structures*, Vol. 46(2), pp. 203-214 (1993)
- Ignatakis, C., Stavrakakis, E. and Penelis, G., Analytical model for masonry using the finite element method, in *Structural Repair and Maintenance of Historical Buildings*, Computational Mechanics Publications, pp. 511-523 (1989)

- Koiter, W.T., Stress-strain relations, uniqueness and variational problems for elastic-plastic materials with a singular yield surface, *Q. Appl. Math.*, Vol. 11, pp. 350-354 (1953)
- Larsson, R., Runesson, K. and Ottosen, N.S., Discontinuous displacement approximation for capturing plastic localization, *Int. J. Numer. Methods Engrg.*, Vol. 36, pp. 2087-2105 (1993)
- Lourenço, P.B. and Rots, J.G., On the use of micro-modelling for the analysis of masonry shear-walls, Proc. 2nd Int. Symp. on Computational Methods in Structural Masonry (Eds. G.N. Pande and J. Middleton), Swansea, U.K. (1993)
- Lourenço, P.B., Rots, J.G. and Blaauwendraad, J., Implementation of an interface cap model for the analysis of masonry structures, Proc. Euro-C Conf. on Computational Modelling of Concrete Structures (Eds. H. Mang, N. Bicanic and R. de Borst), Innsbruck, Austria, Pineridge Press, U.K., pp. 123-134 (1994)
- Mann, W. and Müller, H., Failure of shear-stressed masonry - an enlarged theory, tests and application to shear walls, *Proc. British Ceramic Society*, Vol. 30, pp. 223-235 (1982)
- Maurenbrecker, A.H.P., Effect of test procedures on compressive strength of masonry prisms, Proc. 2nd Canadian Masonry Symp., Canada, pp. 119-132 (1980)
- Ortiz, M. and Popov, E.P., Accuracy and stability of integration algorithms for elastoplastic constitutive relations, *Int. J. Numer. Methods Engrg.*, Vol. 21, pp. 1561-1576 (1985)
- Page, A.W., Finite element model for masonry, *J. Struc. Div.*, ASCE, Vol. 104(8), pp. 1267-1285 (1978)
- Pluijm, R.v.d. and Vermeltfoort, A.Th., Deformation controlled tensile and compressive tests on units, mortar and masonry, report B-91-0561, TNO-BOUW/TU Eindhoven, Building and Construction Research, The Netherlands (in Dutch) (1991)
- Pluijm, R.v.d., Material properties of masonry and its components under tension and shear, Proc. 6th Canadian Masonry Symp., Saskatoon, Canada, pp. (1992a)
- Pluijm, R.v.d., Deformation controlled micro shear tests on masonry samples, Report BI-92-104, TNO-BOUW, Building and Construction Research, The Netherlands (in Dutch) (1992b)
- Pluijm, R.v.d., Shear behaviour of bed joints, Proc. 6th North American Masonry Conf., Philadelphia, U.S.A., pp. 125-136 (1993)
- Pramono, E. and William, K.J., Implicit integration of composite yield surfaces with corners, *Engrg. Comput.*, Vol. 7, pp. 186-197 (1989)
- Priestley, M.J.N. and Elder, D.M., Stress-strain curves for unconfined and confined concrete masonry, *ACI Journal*, Vol. 80(3), pp. 192-201 (1983)
- Raijmakers, T.M.J. and Vermeltfoort, A.Th., Deformation controlled meso shear tests on masonry piers, Report B-92-1156, TNO-BOUW/TU Eindhoven, Building and Construction Research, The Netherlands (in Dutch) (1992)
- Riddington, J.R. and Ghazali, M.Z., Hypothesis for shear failure in masonry joints, *Proc. Instn Civ. Engrs*, Part 2, Vol. 89, pp. 89-102 (1990)
- Riggs, H.R. and Powell, G.H., Tangent constitutive matrices for inelastic finite element analyses, *Int. J. Numer. Methods Engrg.*, Vol. 29, pp. 1193-1203 (1990)

-
- Roscoe, K.H. and Burland, J.B., On the generalized stress-strain behaviour of 'wet' clay, in *Engineering Plasticity*, Edt. by Heyman, J., Lekie, F.A., Cambridge University Press, London, pp. 535-609 (1968)
- Rots, J.G., Computational modelling of concrete fracture, Dissertation, Delft University of Technology, Delft, The Netherlands (1988)
- Rots, J.G., Numerical simulation of cracking in structural masonry, *Heron*, Vol. 36(2), pp. 49-63 (1991)
- Saadeghvaziri, M.A. and Metha, S.S., An analytical model for URM structures, Proc. 6th North American Masonry Conf., Philadelphia, U.S.A., pp. 409-418 (1993)
- Schellekens, J.C.J., Computational strategies for composite structures, Dissertation, Delft University of Technology, Delft, The Netherlands (1992)
- Simo, J.C., Ju, J.W., Pister, K.S. and Taylor, R.L., Assessment of cap model: Consistent return algorithms and rate-dependent extension, *J. Engrg. Mech. Div.*, ASCE, Vol. 114(2), pp. 191-218 (1988a)
- Simo, J.C., Kennedy, J.G. and Govindjee, S., Non-smooth multisurface plasticity and viscoplasticity. Loading/unloading conditions and numerical algorithms, *Int. J. Numer. Methods Engrg.*, Vol. 26, pp. 2161-2185 (1988b)
- Vermeltfoort, A.Th. and Pluimj, R.v.d., Strength and deformation properties of masonry to be used in computer calculations, Proc. 9th Int. Brick/Block Masonry Conf., Berlin, Germany, pp. 244-251 (1991)
- Vermeltfoort, A.Th. and Raijmakers, T.M.J., Deformation controlled meso shear tests on masonry piers, Part 2, Draft report, TU Eindhoven, The Netherlands (in Dutch) (1993)
- Vermeltfoort, A.Th., Raijmakers, Th.M.J. and Janssen, H.J.M., Shear tests on masonry walls, Proc. 6th North American Masonry Conf., Philadelphia, U.S.A., pp. 1183-1193 (1993)
- Vonk, R.A., Softening of concrete loaded in compression, Dissertation, Eindhoven University of Technology, Eindhoven, The Netherlands (1992)

6. APPENDIX A - 3D EXTENSION OF THE CAP MODEL

The extension of the model to a 3D configuration is briefly reviewed here. Under the assumption of isotropic shear behaviour, it is shown that the return mapping can be conveniently carried out in a resultant 2D configuration. By doing so the work of coding the 3D extension of the model is reduced to large extent. For the consistent tangent operator the general formulation derived in Section 4 is applicable and no further derivations are given in this appendix.

The elastic constitutive relation between tractions and relative displacements is given as before by

$$\boldsymbol{\sigma} = \mathbf{D} \boldsymbol{\varepsilon}, \quad (\text{A.51})$$

but for a 3D configuration these quantities read $\mathbf{D} = \text{diag}(k_n, k_s, k_t)$, $\boldsymbol{\sigma} = (\sigma, \tau_s, \tau_t)^T$ and $\boldsymbol{\varepsilon} = (u_n, u_s, u_t)^T$. Again, note that isotropic shear behaviour is assumed.

The composite yield surface that limits the elastic stress space is illustrated in Fig. A.22. The yield surfaces shown (see Section 5) can be rewritten as

$$\begin{cases} f_1(\boldsymbol{\sigma}, \kappa_1) = \sigma - f_t(\kappa_1) \\ f_2(\boldsymbol{\sigma}, \kappa_2) = \sqrt{\tau_s^2 + \tau_t^2} + \sigma \tan \phi(\kappa_2) - c(\kappa_2) \\ f_3(\boldsymbol{\sigma}, \kappa_3) = C_{nn}\sigma^2 + C_{ss}\tau_s^2 + C_{tt}\tau_t^2 + C_n\sigma - \bar{\sigma}^2(\kappa_3) \end{cases}. \quad (\text{A.52a-c})$$

Note that the expressions above are exactly the same as the expressions given for a 2D configuration if the resultant shear stress τ reads

$$\tau = \sqrt{\tau_s^2 + \tau_t^2}. \quad (\text{A.53})$$

For the Coulomb friction mode a non-associated plastic potential g_2 is considered, reading

$$g_2 = \sqrt{\tau_s^2 + \tau_t^2} + \sigma \tan \psi - c. \quad (\text{A.54})$$

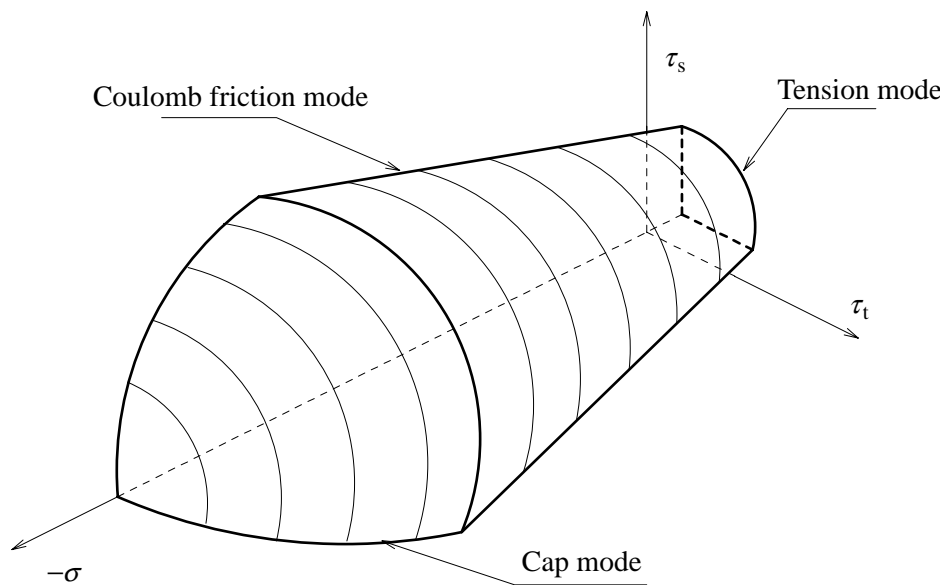


Fig. A.22 - Model for plane interface elements

6.1 Return mapping

Using an implicit Euler backward integration scheme (see Section 4), the return mapping equations read

$$\boldsymbol{\sigma}_{n+1} = \boldsymbol{\sigma}_{n+1}^{\text{trial}} - \Delta\lambda_{n+1} \mathbf{D} \left. \frac{\partial g}{\partial \boldsymbol{\sigma}} \right|_{n+1} . \quad (\text{A.55})$$

For the tension mode the shear components are not present in the yield surface and eq. (A.55) yields simply

$$\begin{cases} \sigma_{n+1} = \sigma^{\text{trial}} - \Delta\lambda_{1, n+1} k_n \\ \tau_{s, n+1} = \tau_s^{\text{trial}} \\ \tau_{t, n+1} = \tau_t^{\text{trial}} \end{cases} . \quad (\text{A.56})$$

For the shear mode the return mapping equation, eq. (A.55), yields

$$\begin{cases} \sigma_{n+1} = \sigma^{\text{trial}} - \Delta\lambda_{2, n+1} k_n \tan \psi \\ \tau_{s, n+1} = \tau_s^{\text{trial}} - \Delta\lambda_{2, n+1} k_s \frac{\tau_{s, n+1}}{\tau_{n+1}} \\ \tau_{t, n+1} = \tau_t^{\text{trial}} - \Delta\lambda_{2, n+1} k_s \frac{\tau_{t, n+1}}{\tau_{n+1}} \end{cases} . \quad (\text{A.57a-c})$$

Eqs. (A.57b,c) can be recast as

$$\begin{cases} \tau_{s, n+1} = \frac{\tau_s^{\text{trial}}}{1 + \frac{\Delta\lambda_{2, n+1} k_s}{\tau_{n+1}}} \\ \tau_{t, n+1} = \frac{\tau_t^{\text{trial}}}{1 + \frac{\Delta\lambda_{2, n+1} k_s}{\tau_{n+1}}} \end{cases} . \quad (\text{A.58})$$

Squaring and adding these equations yields, after some algebra,

$$\tau_{n+1} = \tau^{\text{trial}} - \Delta\lambda_{2, n+1} k_s \quad (\text{A.59})$$

and demonstrates that the return mapping can be carried out in the trial state resultant 2D configuration. Further substitution of eq. (A.59) in eqs. (A.58) yields the updated value of the shear components $\tau_{s, n+1}$ and $\tau_{t, n+1}$,

$$\begin{cases} \tau_{s, n+1} = \tau_{n+1} \frac{\tau_s^{\text{trial}}}{\tau^{\text{trial}}} \\ \tau_{t, n+1} = \tau_{n+1} \frac{\tau_t^{\text{trial}}}{\tau^{\text{trial}}} \end{cases} \quad (\text{A.60})$$

For the cap mode the return mapping equation, eq. (A.55), yields

$$\begin{cases} \sigma_{n+1} = \sigma^{\text{trial}} - \Delta\lambda_{3,n+1} k_n (2\sigma_{n+1} C_{nn} + C_n) \\ \tau_{s,n+1} = \tau_s^{\text{trial}} - 2C_{ss}\Delta\lambda_{3,n+1} k_s \tau_{s,n+1} \\ \tau_{t,n+1} = \tau_t^{\text{trial}} - 2C_{tt}\Delta\lambda_{3,n+1} k_t \tau_{t,n+1} \end{cases} . \quad (\text{A.61a-c})$$

Eqs. (A.61b,c) can be recast as

$$\begin{cases} \tau_{s,n+1} = \frac{\tau_s^{\text{trial}}}{1 + 2C_{ss}\Delta\lambda_{3,n+1} k_s} \\ \tau_{t,n+1} = \frac{\tau_t^{\text{trial}}}{1 + 2C_{tt}\Delta\lambda_{3,n+1} k_t} \end{cases} . \quad (\text{A.62})$$

Squaring and adding these equations yields,

$$\tau_{n+1} = \frac{\tau^{\text{trial}}}{1 + 2C_{ss}\Delta\lambda_{3,n+1} k_s} \quad (\text{A.63})$$

and demonstrates that the return mapping can be carried out in the trial state resultant 2D configuration. Dividing eqs. (A.62) by eq. (A.63) yields the updated value of the shear components $\tau_{s,n+1}$ and $\tau_{t,n+1}$,

$$\begin{cases} \tau_{s,n+1} = \tau_{n+1} \frac{\tau_s^{\text{trial}}}{\tau^{\text{trial}}} \\ \tau_{t,n+1} = \tau_{n+1} \frac{\tau_t^{\text{trial}}}{\tau^{\text{trial}}} \end{cases} . \quad (\text{A.64})$$

For the corners, with the procedure used above, it is straightforward to demonstrate that the return mapping can be carried out in the trial state resultant 2D configuration.

7. APPENDIX B - YIELD SURFACES WITH NON-SEPARATED VARIABLES

The Mohr-circle that corresponds to the ultimate state of stress can be regarded as the natural cap for a Coulomb friction material. Under the habitual assumption that the Coulomb friction law represents, with acceptable accuracy, the envelope of the different failure stress states the cap must be considered tangent to the Coulomb yield surface. As referred in Section 3, masonry is not a homogeneous material. The circular cap does not permit the flexibility of the model described in section 5 and, for this reason, is not used in the body of the present report.

Mohr circular cap (see Fig. B.23) is an example of a yield surface with non-separated variables. This type of yield surfaces leads to more complex algorithms and is seldom used in practice. Here, it is shown that a consistent and robust treatment of this type of yield surfaces is possible.

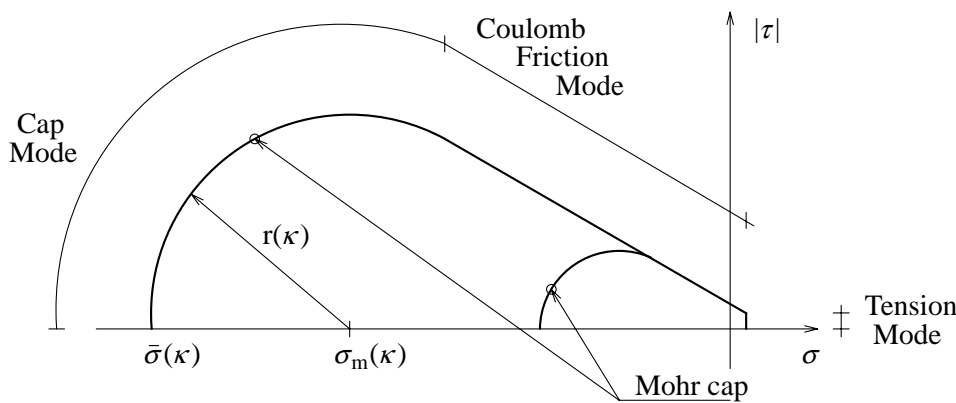


Fig. B.23 - Mohr circular cap model

The Mohr cap yield surface reads

$$f(\boldsymbol{\sigma}, \kappa) = (\sigma - \sigma_m(\kappa))^2 + \tau^2 - r^2(\kappa), \quad (B.65)$$

where the origin σ_m reads

$$\sigma_m = \frac{-\bar{\sigma}(\kappa) + c \cos \phi}{1 + \sin \phi} \quad (B.66)$$

and the radius r ($r > 0$) reads

$$r = \frac{\bar{\sigma}(\kappa) \sin \phi + c \cos \phi}{1 + \sin \phi}. \quad (B.67)$$

Here c is the cohesion and ϕ is the friction angle. The yield value $\bar{\sigma}$ is conveniently defined as the uniaxial compressive strength, see Section 5 (Fig. 23) for the assumed $\bar{\sigma} - \kappa$ diagram.

Defining the new origin or back stress, $\boldsymbol{\alpha}(\kappa)$, as

$$\boldsymbol{\alpha} = (\sigma_m(\kappa), 0)^T \quad (B.68)$$

and the reduced stress $\boldsymbol{\eta}(\boldsymbol{\sigma}, \kappa)$ as

$$\boldsymbol{\eta} = \boldsymbol{\sigma} - \boldsymbol{\alpha}(\kappa), \quad (B.69)$$

the Mohr cap yield surface, cf. eq.(B.1), can be rewritten as

$$f(\boldsymbol{\sigma}, \kappa) = [\boldsymbol{\eta}(\boldsymbol{\sigma}, \kappa)]^T \boldsymbol{\eta}(\boldsymbol{\sigma}, \kappa) - r^2(\kappa). \quad (B.70)$$

Then, the elastoplastic equations that govern the material behaviour read, in the case of strain hardening/softening and associated flow,

$$\boldsymbol{\varepsilon} = \boldsymbol{\varepsilon}^e + \boldsymbol{\varepsilon}^p \quad (\text{B.71a})$$

$$\boldsymbol{\sigma} = \mathbf{D}\boldsymbol{\varepsilon}^e \quad (\text{B.71b})$$

$$\dot{\boldsymbol{\varepsilon}}^p = 2\lambda\boldsymbol{\eta} \quad (\text{B.71c})$$

$$\dot{\kappa} = 2\dot{\lambda}\mathbf{r} \quad (\text{B.71d})$$

$$f = \boldsymbol{\eta}^T \boldsymbol{\eta} - \mathbf{r}^2 \leq 0. \quad (\text{B.71e})$$

If a squared formulation for the yield function is considered instead of the quadratic formulation, eq. (B.71d) reads

$$\dot{\kappa} = \dot{\lambda}. \quad (\text{B.72})$$

This expression alleviates the formulation but will not be considered here for two reasons. Firstly, the objective of this appendix is to introduce a general methodology and, secondly, the gradient of the squared formulation is not defined when softening is completed ($\kappa \rightarrow \infty$).

7.1 Algorithm implementation

Using an implicit Euler backward return mapping, the stress update reads

$$\boldsymbol{\sigma}_{n+1} = \boldsymbol{\sigma}^{\text{trial}} - 2\Delta\lambda_{n+1}\mathbf{D}\boldsymbol{\eta}_{n+1} = \boldsymbol{\sigma}^{\text{trial}} - 2\Delta\lambda_{n+1}\mathbf{D}(\boldsymbol{\sigma}_{n+1} - \boldsymbol{\alpha}_{n+1}) \quad (\text{B.73})$$

and can be recast as

$$\boldsymbol{\sigma}_{n+1} = (\mathbf{I} + 2\Delta\lambda_{n+1}\mathbf{D})^{-1}(\boldsymbol{\sigma}^{\text{trial}} + 2\Delta\lambda_{n+1}\mathbf{D}\boldsymbol{\alpha}_{n+1}). \quad (\text{B.74})$$

A simple inspection of eq. (B.71d) shows that a local iterative Newton method to solve the return mapping cannot be performed in terms of $\Delta\lambda_{n+1}$. If eq. (B.71d) is rewritten, for finite increments, as

$$\Delta\lambda_{n+1} = \frac{\Delta\kappa_{n+1}}{2\mathbf{r}_{n+1}}, \quad (\text{B.75})$$

and substituted in eq. (B.74), further substitution in the yield function leads to a non-linear equation in one variable, namely $\Delta\kappa_{n+1}$: $f_{n+1}(\Delta\kappa_{n+1}) = 0$. This constitutive equation is solved here with a local Newton method. The derivative of $f_{n+1}(\Delta\kappa_{n+1})$ with respect to $\Delta\kappa_{n+1}$, which is needed in this procedure, reads

$$\left. \frac{\partial f}{\partial \Delta\kappa} \right|_{n+1} = 2\boldsymbol{\eta}_{n+1}^T \frac{d\boldsymbol{\eta}}{d\Delta\kappa} - 2\mathbf{r}_{n+1} \frac{\partial \mathbf{r}}{\partial \Delta\kappa}, \quad (\text{B.76})$$

where

$$\frac{d\boldsymbol{\eta}}{d\Delta\kappa} = \frac{d\boldsymbol{\sigma}}{d\Delta\kappa} - \frac{\partial \boldsymbol{\alpha}}{\partial \Delta\kappa}. \quad (\text{B.77})$$

Note that $\boldsymbol{\sigma}_{n+1} = \boldsymbol{\sigma}_{n+1}(\Delta\lambda_{n+1}, \Delta\kappa_{n+1}, \boldsymbol{\alpha}_{n+1})$, $\Delta\lambda_{n+1} = \Delta\lambda_{n+1}(\Delta\kappa_{n+1})$ and $\boldsymbol{\alpha}_{n+1} = \boldsymbol{\alpha}_{n+1}(\Delta\kappa_{n+1})$.

7.2 Consistent tangent operator

The consistent tangent operator \mathbf{D}^{ep} can be easily derived from the algorithmic form of the elastoplastic equations as done in Section 4 and reads

$$\mathbf{D}^{ep} = \left. \frac{d\boldsymbol{\sigma}}{d\boldsymbol{\varepsilon}} \right|_{n+1} = \mathbf{H}^{-1} - \frac{\mathbf{H}^{-1} \bar{\boldsymbol{\gamma}} \left(\frac{\partial f}{\partial \boldsymbol{\sigma}} \right)^T \mathbf{H}^{-1}}{\mathbf{h} + \left(\frac{\partial f}{\partial \boldsymbol{\sigma}} \right)^T \mathbf{H}^{-1} \bar{\boldsymbol{\gamma}}}, \quad (\text{B.78})$$

where the modified compliance matrix \mathbf{H} is given, as usual, by

$$\mathbf{H} = \mathbf{D}^{-1} + \Delta\lambda_{n+1} \frac{\partial^2 f}{\partial \sigma^2}, \quad (\text{B.79})$$

the modified plastic potential gradient $\bar{\gamma}$ reads

$$\bar{\gamma} = \frac{\partial f}{\partial \sigma} + \Delta\lambda_{n+1} \frac{\partial^2 f}{\partial \sigma \partial \kappa} \frac{\partial \kappa}{\partial \Delta\lambda} \quad (\text{B.80})$$

and the hardening modulus reads

$$h = 2 \left(\boldsymbol{\eta}_{n+1}^T \frac{\partial \alpha}{\partial \kappa} + r_{n+1} \frac{\partial r}{\partial \kappa} \right) \frac{\partial \kappa}{\partial \Delta\lambda}. \quad (\text{B.81})$$

7.3 Verification of the model. One element tests

The performance of the cap described above is now evaluated as in Section 5.3. The efficiency of the return mapping is verified in a one element test in uniaxial compression. The results are shown in Table B.3. Note that the results shown before for the elliptical cap are reproduced here to facilitate the comparison between both algorithms. With the local Newton method quadratic convergence is obtained when sufficiently close to the solution. The secant method is also able to locate the solution even if very large steps are considered but, on average, with 40% more local iterations.

Table B.3 - Number of local iterations per global iteration for cap mode

Steps	Mohr cap		Elliptical cap	
	Local Newton method	Local secant method	Local Newton method	Local secant method
100	5.36	7.18	4.54	5.90
10	8.94	12.74	7.56	10.26
2	12.56	18.11	11.00	15.22

The efficiency of the global Newton-Raphson is verified in a one element test under arbitrary loading, see Fig. B.24. A load is applied with direct displacement control as in Section 5.3. Three different step sizes are considered by dividing the displacement that corresponds to the final load in 100, 10 and 2 equal increments.

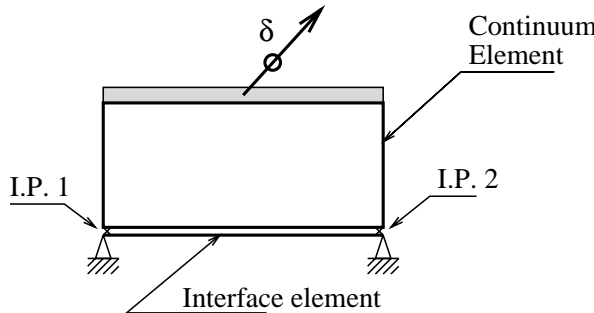


Fig. B.24 - One element test with general loading

The displacement δ shown in Fig. B.24 was chosen equal to $(1/\sqrt{2}, -1/\sqrt{2})$. Fig. B.25 illustrates the force-displacement response. Here \underline{F} is the resultant force in the δ direction. Table B.4 and Table B.5 show the return mapping and the global structural performance. By using a tangent operator consistent with the integration algorithm quadratic convergence is obtained at the structural level.

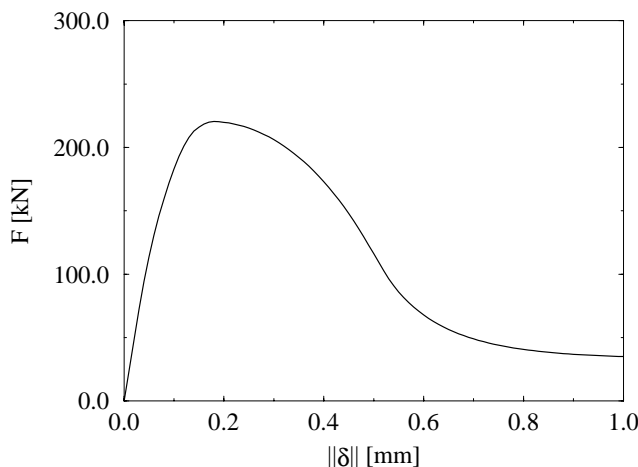


Fig. B.25 - Force/displacement diagram

Table B.4 - Results for general loading

Steps	Local iterations per global iteration		Global iterations	
	Local Newton method	Local secant method	Maximum	Average
100	6.01	8.19	3	1.96
10	10.13	14.09	3	2.20
2	14.39	20.72	4	3.50

Table B.5 - Convergence for selected steps

Test 1 - 100 steps			
Step	I.P.1	I.P.2	Energy norm
3	Elastic	Plastic	0.521×10^{-5} 0.604×10^{-11}
4	Plastic	Plastic	0.706×10^{-3} 0.323×10^{-7} 0.812×10^{-16}
100	Plastic	Plastic	0.746×10^{-8}

Test 2 - 10 steps			
Step	I.P.1	I.P.2	Energy norm
1	Plastic	Plastic	0.571×10^{-1} 0.122×10^{-3} 0.123×10^{-8}
20	Plastic	Plastic	0.186×10^{-4} 0.684×10^{-15}

Test 3 - 2 steps			
Step	I.P.1	I.P.2	Energy norm
1	Plastic	Plastic	0.659×10^0 0.176×10^{-2} 0.236×10^{-6} 0.119×10^{-13}
2	Plastic	Plastic	0.165×10^0 0.164×10^{-6} 0.524×10^{-17}